

# GENERATION OF THE MAGNETIC NULL FIELD TOPOGRAPHY IN A NOVEL ELECTRIC PROPULSION PROOF-OF-CONCEPT

CHARLES L. KELLY, '14

SUBMITTED TO THE  
DEPARTMENT OF MECHANICAL AND AEROSPACE ENGINEERING  
PRINCETON UNIVERSITY  
IN PARTIAL FULFILLMENT OF THE REQUIREMENTS OF  
UNDERGRADUATE INDEPENDENT WORK.

FINAL REPORT

MAY 1, 2014

EDGAR Y. CHOUERI  
SZYMON SUCKEWER  
MAE 442D  
69 PAGES  
FILE COPY

© Copyright by Charles L. Kelly, 2014.  
All Rights Reserved

This thesis represents my own work in accordance with University regulations.

# Abstract

An experimental device to prove the feasibility of a novel plasma propulsion concept utilizing beating electrostatic waves to accelerate ions in a polarity-reversing rectilinear magnetic field is designed, built, and tested. The electromagnetic coils in the device are designed around criteria determined by the ion dynamics. The magnetic field generated is shown to closely match its proposed profile used in earlier experiment-qualifying simulations of the thruster's ion dynamics. Due to its Helmholtz-like geometry, the device may be scaled linearly without affecting the field topography or the absolute size of the magnetic reversal. A specific definition of field uniformity is drawn and used to revise the mathematical construction of the field topography with a new scaling parameter  $\sigma$  to recreate a high-fidelity profile with any desired magnetic reversal size. Simulations using both this construct and the measured field of the device indicate a positive relation between performance and relative size of the thruster chamber to ion gyroradius, determined by magnetization or device scale. Two experimental attempts at measuring an ion current exiting the thruster fail due to massive wall losses inside the chamber, lending credence to the simulations showing poor performance in small thruster sizes.

# Acknowledgements

First and foremost, thank you Mom and Dad for affording me the opportunity to attend Princeton and study what excites me. You have always supported me in every decision I've made and challenge I've faced and for that I will always be grateful.

Thank you Professor Choueiri for not only allowing me to work in the EPPDyL for the past year but for giving me total freedom and trusting me in my research. Thank you Matthew Feldman for being a continual guiding force and teaching me everything I know about plasma physics, even if that isn't much. Thank you Bob Sorenson for having the patience to actually work with me on building this device. Thank you Justin Little for not only generously allowing me to use your experiment but also taking the time to oversee and help with my entire experimental process. Thank you Jo Ann for your superhuman ability to keep us from imploding.

Thank you Will Gillis and Teddy Schleifer for leaving an indelible mark on my Princeton experience and my life more generally. Gonna miss you over break. Thank you Nina Masters for always being there to commiserate over our relegation to the depths of the E-Quad, among other things. Thank you Farhan Abrol for your everlasting friendship and so that you might share some of your inevitable fortune with me.

Thank you to the Program in Plasma Science and Technology, the Mechanical and Aerospace Engineering Department, and the School of Engineering and Applied Sciences for providing funding for this research.



Self discipline  
Self motivation  
Self determination  
Self confidence  
Self perseverance

# Contents

Abstract . . . . .	iii
Acknowledgements . . . . .	iv
List of Tables . . . . .	viii
List of Figures . . . . .	ix
<b>1 Introduction</b>	<b>1</b>
1.1 Goal of This Thesis . . . . .	1
1.2 Fundamentals of Rocket Propulsion . . . . .	1
1.2.1 Implications . . . . .	2
1.3 Modern Electric Propulsion . . . . .	3
1.4 MagNul as a Propulsion Concept . . . . .	3
1.4.1 Advantages Over Current Technology . . . . .	3
1.4.2 Anticipated MagNul Performance . . . . .	3
1.4.3 Motivation for Laboratory Testing of MNT . . . . .	4
1.5 Organization of This Thesis . . . . .	4
<b>2 MagNul Overview</b>	<b>6</b>
2.1 Beating Wave Mechanism . . . . .	6
2.2 Magnetic Field Topography . . . . .	7
2.3 Ion Dynamics . . . . .	8
2.3.1 Normalization Scheme . . . . .	9
2.3.2 Unperturbed Dynamics ( $\varepsilon = 0$ ) . . . . .	10
2.3.3 Perturbed Dynamics ( $\varepsilon > 0$ ) . . . . .	14
<b>3 Proof-of-Concept MagNul Design</b>	<b>17</b>
3.1 Design Criteria . . . . .	17
3.1.1 Uniform Field Region . . . . .	17
3.1.2 Magnetic Reversal Width . . . . .	19
3.2 Design of Coils . . . . .	19

3.2.1	Coil System . . . . .	19
3.2.2	Construction of Coil System . . . . .	20
3.2.3	Magnetic Field Generated . . . . .	22
3.3	Thruster Chamber . . . . .	24
<b>4</b>	<b>Results and Discussion</b>	<b>29</b>
4.1	Revised Mathematical Construct . . . . .	29
4.2	Magnetization and Performance . . . . .	30
4.2.1	Performance Simulations . . . . .	31
4.2.2	Implications . . . . .	32
4.3	Proof-of-Concept Experiment . . . . .	37
4.3.1	Experimental Setup . . . . .	37
4.3.2	Experimental Results . . . . .	38
4.3.3	Sources of Failure . . . . .	39
4.4	Future Work . . . . .	41
4.5	Concluding Remarks . . . . .	42
<b>A</b>	<b>Calculation of Plasma Fan</b>	<b>47</b>
<b>B</b>	<b>Derivation of Scaling Parameter <math>\sigma</math></b>	<b>50</b>
<b>C</b>	<b>Experiment Pictures</b>	<b>52</b>

# List of Tables

4.1	Monte Carlo numerical simulation results for varying levels of magnetization. . . . .	32
4.2	Performance results of varying sizes of mathematical reconstructions of the magnetic null topography for $\bar{r}_L = 1$ cm ( $B_0 = 360$ Gauss). . .	36

# List of Figures

2.1	A simplified view of the Magnetic Null field topography. Two opposing uniform regions sit above and below the magnetic null plane (blue) at $Y = 0$ . Straight arrows indicate field lines. Curved arrows represent direction of current in the coils drawn.[7]	7
2.2	$B_0$ -normalized magnetic null field topography with $\delta = 1$ .	8
2.3	The mechanism by which the magnetic null works to direct ions in $+\hat{\mathbf{x}}$ . [7]	9
2.4	LB trajectories ( $P_X > 0$ ). Higher $H$ results in a more linear path.[12]	12
2.5	Trajectories for ions with $P_X = -5.8$ . As $H$ is increased, trajectories open up and approach LB.[12]	13
2.6	Trajectory classification of an ion based on its initial $H$ and $P_X$ . [12]	14
3.1	Electromagnetic coil system for generating magnetic null topography. Current direction is indicated by blue lines.	21
3.2	Electromagnetic coil system in the position it sits on the test stand.	22
3.3	Device to generate the magnetic null field topography. The blue box outlines the exit of the thruster chamber region.	23
3.4	Magnetic field generated between the middle two pairs of coils (the thruster chamber). The outlined borders represent the shape of the coils. The red uniform region field lines point in $+\hat{\mathbf{z}}$ while the blue points in $-\hat{\mathbf{z}}$ . Green is a field strength of 0. (The color scale has been omitted intentionally since it included arbitrary field strength values).	24
3.5	Comparison of the theoretical magnetic null topography with $\delta = 1.5$ cm and $\sigma = 1.72$ (red), the topography generated by the coil system in simulations (black), and the field generated by the physical coil system (blue).	25
3.6	Magnitude of drift velocity $V_d$ in $\hat{\mathbf{x}}$ for $\bar{r}_L = 1$ cm. The gray line represents $V_{d,max}$ ; the regions in $Y$ below this line are the uniform regions.	25

3.7	Comparison of the magnetic field generated when using ferrite in the main two coil pairs (black) and the field generated without ferrite (red).	26
3.8	Relationship between $\bar{\delta}$ and $B_0$ . For $\bar{\delta} = 1$ , $B_0 = 240$ Gauss. . . . .	26
3.9	Glass chamber constructed for this experiment with its characteristic “duck-billed” shape. It is covered in a copper mesh to prevent stray RF outside the plasma source, which will be inside the cylindrical region as close to the swept blend as possible. In this image, the blended adapter section is wound with extra coils to magnetically confine the plasma; this will be discussed in Chapter 4. . . . .	28
4.1	Comparison of the $\nabla B$ drift in the actual device (black) and the theoretical reconstruction of the device (red). The gray line marks $V_{d,max}$ . The region of uniformity begins at exactly the same $Y$ for both the generated field and its mathematical reconstruction. . . . .	30
4.2	Color map of the eventual exit velocity of an ion as a function of its initial position $(X, Y)$ in the heated, high magnetization case ( $B_0 = 705$ Gauss, $\bar{\delta} = 3$ ). Lighter blue represents higher exit velocity. Empty white space represents ions that have been lost to the walls. $\varepsilon = 10$ , $\kappa = 0.16$ , $\nu = 1.47$ . . . . .	33
4.3	Color map of the eventual exit velocity of an ion as a function of its initial position $(X, Y)$ in the heated, low magnetization case ( $B_0 = 176$ Gauss, $\bar{\delta} = 0.75$ ). Lighter blue represents higher exit velocity. Empty white space represents ions that are trapped or have been lost to the walls. $\varepsilon = 10$ , $\kappa = 0.16$ , $\nu = 1.47$ . . . . .	34
4.4	$\xi_{tr}$ (black), $\xi_{ex}$ (red), and $\xi_{lost}$ (blue) in the perturbed case at varying field strengths. . . . .	35
4.5	$I_{sp}$ in s versus $B_0$ in Gauss. There is a clear peak in thruster performance near 5000 Gauss. . . . .	36
4.6	Color map of the eventual exit velocity of an ion as a function of its initial position $(X, Y)$ in the heated case. The field was mathematically defined using $\sigma = 1.72$ and $\bar{\delta} = 1.5$ to faithfully reconstruct the thruster magnetic field with $y_{max} = 6$ cm. . . . .	37

4.7	Color map of the eventual exit velocity of an ion as a function of its initial position $(X, Y)$ in the heated case. The field was mathematically defined using $\sigma = 1.72$ and $\bar{\delta} = 1.5$ to faithfully reconstruct the thruster magnetic field with $y_{max} = 15$ cm, a scaled up version of the thruster built for the experiment. . . . .	38
4.8	Magnetic field lines (blue) diverging away from $\hat{\mathbf{z}}$ tilt the Larmor orbits of ions, increasing their chance of hitting a wall. . . . .	40
4.9	$\theta(z)$ (red) and the actual divergence of the uniform field lines (black) for $\bar{r}_L = 1.5$ cm. The field divergence only exceeds $\theta$ very close to the walls, causing roughly 13% of the plasma to be lost. . . . .	41
4.10	View along the thrust axis of a potential annular MagNul. Field-generating coils (orange) placed around a ring generate a cylindrical null sheet (red). Blue arrows indicate direction of field lines. . . . .	43
C.1	Side view from $+\hat{\mathbf{y}}$ of thruster setup on test stand. Plasma flows from right to left in this image. Plasma source and RF antenna can be seen entering the cylindrical section of the duck-billed glass tube. The injection backplate lies just to the right of the beginning of the confinement windings. Due to an error made by the glass-blowing shop, the chamber extends about 1" short of the end of the magnets. . . . .	52
C.2	View from the exit-side of the thruster. Plasma would be exiting towards the viewer in this image. . . . .	53
C.3	View from exit-side of the thruster showing the plasma source and generator (top left), the thruster chamber and field generator, and Faraday and Langmuir probes in plume region. . . . .	53
C.4	Plasma injection into the thruster region without magnetic confinement coils. Image taken from the $-\hat{\mathbf{y}}$ side. . . . .	54
C.5	Plasma penetration into the thruster region at low density and RF power without magnetic confinement coils. This image was taken from $+\hat{\mathbf{y}}$ ; plasma flow is from right to left. The gray streak is the plasma inside the rectangular chamber region; the G10 standoff partially obscuring the plasma, about 1 cm wide, gives a sense of the length scale. All plasma is lost after roughly 2 cm. . . . .	55

C.6	Plasma injection into the thruster region without magnetic confinement coils. Image taken from the $+\hat{y}$ side. The G10 standoff obscuring the plasma in Figure C.5 can be seen more clearly in this image, taken from the same vantage point. . . . .	55
C.7	Plasma injection into the thruster chamber with magnetic confinement coil. The RF antenna sitting behind the backplate inside the cylindrical section can be seen clearly. Taken from the $-\hat{y}$ side. . . . .	56
C.8	View from $+\hat{y}$ of the plasma penetration into the thruster region. The plasma makes it about halfway through the chamber (or 6 cm) before being completely lost to the walls. . . . .	57
C.9	Operation of the MagNul with magnetic confinement at high RF power and density. . . . .	57



# Chapter 1

## Introduction

### 1.1 Goal of This Thesis

This thesis aims to design, construct, and test a proof-of-concept for a novel plasma propulsion technique utilizing beating electrostatic waves (BEW) to accelerate ions across a magnetic field reversal. It is hoped that this Magnetic Null Thruster (MagNul) will match or exceed the performance of existing flight-proven electric propulsion devices. The following is the first attempted laboratory exploration of the plasma dynamics in the magnetic field employed by the MagNul that will help determine its feasibility as an operational electric propulsion device. It is also the first physical generation of the magnetic null field topography. Although the BEW heating mechanism is not employed in this experiment, the constructed device is designed for its eventual use.

### 1.2 Fundamentals of Rocket Propulsion

We primarily characterize rocket performance by thrust  $T$  and specific impulse  $I_{sp}$ . Rocket thrust is generated from the momentum change achieved by accelerating the propellant. In a rocket where some propellant of mass  $m$  is accelerated to an exit velocity  $u_e$ , the thrust can thus be expressed as

$$T = \dot{m}u_e \tag{1.2.1}$$

which is simply an expression of the time change in momentum  $mu_e$ <sup>1</sup>.  $I_{sp}$  is a measure of impulse per unit weight of propellant and is simply

$$I_{sp} = \frac{u_e}{g_0} \quad (1.2.2)$$

where  $g_0$  is the acceleration due to gravity at sea level.  $I_{sp}$  has units of time (s). The physical meaning of  $I_{sp}$  is not unlike fuel efficiency; higher  $I_{sp}$  corresponds to a more fuel efficient rocket in terms of thrust generation over time (e.g. a rocket with  $I_{sp} = 300$  s can produce 1 N of thrust per 1 kg of propellant continuously for 300 s).

The Rocket Equation relates  $\Delta v$  to the propellant mass fraction of the vehicle<sup>2</sup>. This is written as

$$\frac{m_p}{M_0} = 1 - e^{-\frac{\Delta v}{u_e}} \quad (1.2.3)$$

where  $m_p$  is the propellant mass used in the burn and  $M_0$  is the total initial mass of the vehicle. Thus for any rocket whose  $u_e$  is known, we have a direct relation between the  $\Delta v$  of a burn and the  $m_p$  required to achieve it.

### 1.2.1 Implications

The Rocket Equation, though simple, has grand implications for propulsion. Since desired  $\Delta v$  defines the spacecraft propulsion subsystem requirements and is independent of vehicle mass or rocket type, we generally optimize it for minimum fuel requirement. From equation 1.2.3 it is clear that the propellant mass fraction may be reduced by increasing  $u_e$ . The benefit of an increase in exhaust velocity then is threefold since both  $T$  and  $I_{sp}$  scale linearly with  $u_e$ .

As a result, rocket engineers seek ways to accelerate propellants to higher exhaust velocities. Chemical/thermal propulsion is limited in this regard; since the acceleration is driven by the chemical energy released in combustion,  $u_e$  is limited by the energy density of propellants. Electric propulsion sidesteps this limitation by accelerating ionized gases via magnetic and/or electric body forces<sup>3</sup>, with its primary performance limitation being the power available on board the spacecraft. Using these techniques, electric thrusters achieve far higher exhaust velocities (and subsequently specific impulses), opening the door to high  $\Delta v$  missions without inordinate

---

<sup>1</sup>The initial velocity of the propellant  $u_0 \ll u_e$ , therefore the velocity change of the propellant is just the absolute exit velocity  $u_e$ .

<sup>2</sup> $\Delta v$  is a measure of the velocity change imparted on a vehicle over the duration of a rocket burn.

<sup>3</sup>Electric propulsion also includes those thrusters that electrically heat propellants; such electrothermal devices are the cross section between thermal and electric propulsion.

fuel usage. This makes them ideal candidates for interplanetary missions[21].

## 1.3 Modern Electric Propulsion

Electrothermal devices like resistojets and arcjets can achieve specific impulses between 250–850 s and 1000–2000 s respectively[11]. Other flight-proven devices fare better; Hall thrusters can exceed 3000 s[17] while ion thrusters can get up to 9000 s[11]. Magnetoplasmadynamic thrusters range from 1000–6500 s and are very efficient at high power levels[11][22][1]. The disadvantage of electric propulsion devices is their low thrust, usually on the order of  $\mu\text{N}$  to a few N.

These  $I_{sp}$  values are considerably better than those seen in chemical rockets: a very large rocket such as the J-2 used on Saturn V, with thrust exceeding 1 MN, has a specific impulse of 420 s[18]; cold gas micro-thrusters used for attitude control have thrust levels comparable to their electric counterparts but with  $I_{sp} < 100$  s[14].

## 1.4 MagNul as a Propulsion Concept

### 1.4.1 Advantages Over Current Technology

The MagNul presents several advantages over chemical propulsion options and even other electric propulsion devices. It has considerably higher fuel efficiency than chemical rockets, with potential specific impulse exceeding 1000 s. The  $I_{sp}$  and thrust may be varied manually by controlling the beating wave parameters (thereby controlling the acceleration of ions). Additionally, the lifetime of the thruster is not limited by electrode erosion as it is electrodeless; this is one of the primary limiting factors in currently used electric thrusters[22][24]. The MagNul also preferentially transports ions away from the walls of the thruster, meaning it will not experience the same levels of recombination and energy loss to the wall seen in other thrusters[2].

### 1.4.2 Anticipated MagNul Performance

The mechanisms behind and a proposed proof-of-concept for the MagNul were first laid out in 2010 by Jorns and Choueiri[12] and further explored numerically in 2011 by Gardineer et al[10]. These works provide the foundation for the MagNul, qualifying its construction with theoretical performance metrics and data.

Gardineer showed in simulations that the MagNul operating with Argon gas as propellant would have a specific impulse of 1500 s, thrust density of 70 mN/m, and an average exhaust velocity of 14.5 km/s[10]. With hydrogen gas propellant the  $I_{sp}$  jumps to 9500 s. These values indicate that the MagNul will have comparable performance to many existing electric propulsion devices. It is clear that the MagNul theoretically meets the performance benchmarks required for viability as a plasma thruster.

### 1.4.3 Motivation for Laboratory Testing of MNT

These numerical results, while promising, leave many questions that may only be answered in a laboratory setting. The ion density used for computations is orders of magnitude lower than that experienced in real thrusters; this combined with the computational complexity of such considerations means collisional effects have been ignored. It is possible that collisional effects will harm the thruster performance by decreasing the ion Hall parameter of the plasma<sup>4</sup>[10] or by transporting plasma to the walls. Additionally, electron dynamics have only been considered independently from ion dynamics[7]; as of yet, no self-consistent simulations of plasma dynamics in the magnetic null topography have been published. Such simulations exceed modern practical computational ability without applying the same simplifications to density and collisional considerations, thus observing these dynamics in a laboratory setting should prove not only more reliable but more feasible than predicting them numerically. Various other assumptions were made in previous analyses that contribute to the potential inaccuracy that will be resolved upon testing a device with real-world limitations and capabilities.

## 1.5 Organization of This Thesis

Chapter 2 will give an overview of the MagNul propulsion concept, introducing the two primary components: the magnetic null field topography and the beating wave heating mechanism. We will explore the ion dynamics governed by these two aspects. Some preliminary implications of these dynamics for thruster design will be discussed. We will look at results from previous theoretical simulations to qualify the need for a physical test of the device. In chapter 3, we will outline the design criteria

---

<sup>4</sup>In the next chapter we will see that the MagNul relies heavily on unimpeded ion cyclotron motion, requiring that the ion Hall parameter  $\Omega_i \gg 1$ .

for the proof-of-concept experiment. Each aspect of the design will be presented and discussed. We will compare measurements of the generated magnetic field to the proposed theoretical field used in previous performance simulations. The final chapter will detail the results of the experimental attempts at a proof-of-concept. We will also introduce a revision of the theoretical construction of the magnetic null topography. Finally, we will propose methods to improve the design and outline future work.

# Chapter 2

## MagNul Overview

### 2.1 Beating Wave Mechanism

In 1998, a mechanism by which magnetized ions are accelerated using a spectrum of electrostatic waves propagating perpendicular to the magnetic field was proposed by Ram et al[20]. This acceleration technique was shown to coherently energize ions whose velocities were substantially lower than the phase velocity of the individual waves, improving upon single electrostatic wave (SEW) acceleration whose lower bound on energizable ions is those with velocity equal to the wave phase velocity[13]. Further, Benisti et al. showed that these ions may be accelerated from arbitrarily low initial energies[3] and that the acceleration was enhanced when at least two waves were on-resonant with the ion cyclotron frequency[4], i.e.

$$\omega_1 - \omega_2 = n\omega_{c,i} \quad (2.1.1)$$

where  $n$  is an integer,  $\omega_1$  and  $\omega_2$  are the frequencies of the propagating electrostatic waves, and  $\omega_{c,i}$  is the ion cyclotron frequency. Equation 2.1.1 is known as the beating condition and two waves that meet this criterion are eponymously Beating Electrostatic Waves (BEW)<sup>1</sup>. Spektor and Choueiri noted that the arbitrarily large accelerations posited by Benisti et al. are limited to certain regions in phase space defined by the initial hamiltonian of the ion<sup>2</sup>[23]. Despite these “necessary and sufficient” conditions placed on their acceleration profile, BEW are still found to substantially

---

<sup>1</sup>Off-resonant waves may still be called beating waves; for our purposes, BEW will refer solely to the on-resonant case as this will become our ion acceleration mechanism.

<sup>2</sup>These conditions are examined in section 2.3.3.

lower the threshold at which a magnetized ion may be energized compared to the case of SEW.

## 2.2 Magnetic Field Topography

The magnetic field configuration of the MagNul is central to its effectiveness at generating thrust. It acts as the primary mechanism by which an ion current is established directionally out of the thruster. It consists of two equal and opposite regions of uniform field strength atop one another. Between the regions is a steeply-sloped gradient over which the field reverses direction. The plane at the point of reversal is said to be the magnetic null and has no magnetic field. An illustration of the field is seen in Figure 2.1.

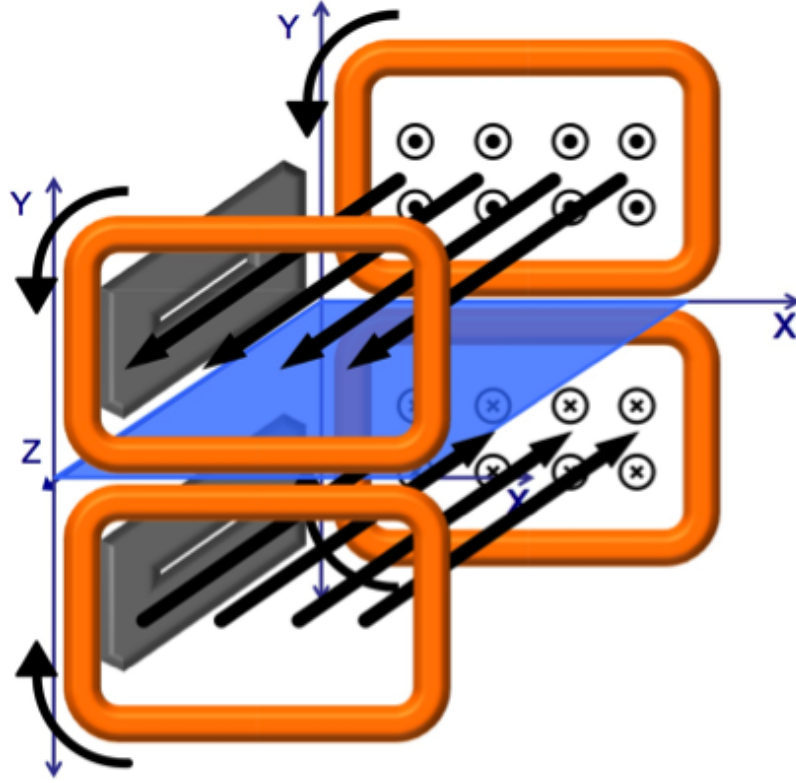


Figure 2.1: A simplified view of the Magnetic Null field topography. Two opposing uniform regions sit above and below the magnetic null plane (blue) at  $Y = 0$ . Straight arrows indicate field lines. Curved arrows represent direction of current in the coils drawn.[7]

We construct the magnetic null mathematically by orienting the field lines along  $\hat{z}$  (the unit vector along the  $z$ -axis) as a function of  $y$  (coordinate system as defined

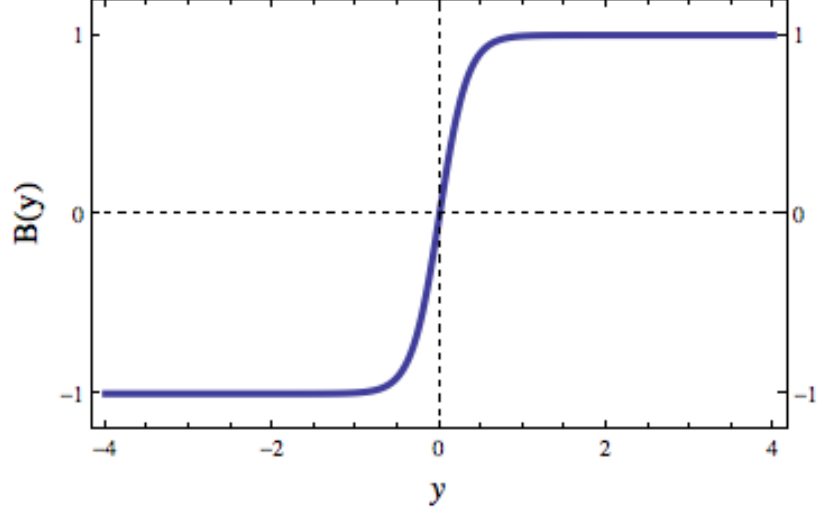


Figure 2.2:  $B_0$ -normalized magnetic null field topography with  $\delta = 1$ .

in Figure 2.1). The sloped region occupies  $|y| \leq \delta$  where  $\delta$  is the magnetic reversal half-width, leaving the null plane at  $y = 0$ . The uniform region occupying  $|y| > \delta$  has field strength  $B_0$ . The hyperbolic tangent function, represented graphically in Figure 2.2, is scaled to yield these properties[12]:

$$\mathbf{B}(y) = B_0 \tanh \frac{3y}{\delta} \hat{\mathbf{z}} \quad (2.2.1)$$

## 2.3 Ion Dynamics

Figure 2.3 shows a simplistic view of how this field topography works to produce an ion current. Ions in the uniform regions exhibit characteristic Larmor orbiting whose direction is determined by the Lorentz force[5]; in our formulation this manifests as clockwise orbits for  $+\hat{\mathbf{z}}$  field lines and counterclockwise for  $-\hat{\mathbf{z}}$  field lines. If an ion is near enough to the null plane for its orbit to cross it, the orbit direction will reverse, sending it on a mirrored-orbit trajectory with net motion in the  $+\hat{\mathbf{x}}$  direction. All such ions will remain in this  $+\hat{\mathbf{x}}$  trajectory indefinitely; for our purposes, these ions exit the thruster. Though this is the primary mechanism of thrust generation in the MagNul, there are other trajectories an ion may follow that can result in counterproductive  $-\hat{\mathbf{x}}$  net motion. The dynamics governing all possible trajectories will be explored below.



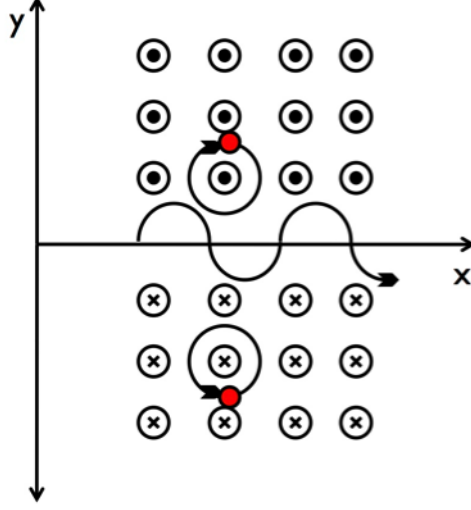


Figure 2.3: The mechanism by which the magnetic null works to direct ions in  $+\hat{\mathbf{x}}$ . [7]

### 2.3.1 Normalization Scheme

Jorns and Choueiri[12] give the Hamiltonian of a magnetized ion interacting with multiple electrostatic waves by adapting that derived by Chia[6]. The Hamiltonian  $h$  governing the motion of such an ion is

$$h = \frac{1}{2} [(p_x - qA_x)^2 + p_y^2] + \frac{qE_0}{k} \sum_{i=1,2} \cos(kx - \omega_i t) \quad (2.3.1)$$

whose symbols have the following meanings:

- $\mathbf{A}$  = magnetic vector potential
- $p_x$  =  $m\dot{x} + qA_x$  for particle mass  $m$
- $p_y$  =  $m\dot{y}$  for particle mass  $m$
- $q$  = charge
- $E_0$  = electric field amplitude
- $k$  = wave number
- $\omega_i$  = frequency of  $i^{th}$  wave satisfying equation 2.1.1 for  $n = 1$
- $t$  = time

Gardineer[10] rewrites the Hamiltonian following an  $\bar{r}_L$ -normalization scheme where

$\bar{r}_L$  is the root-mean-square Larmor radius of the ion ensemble. Normalizing length to  $\bar{r}_L$  and time to  $\omega_{c,i}^{-1}$  we have

$$H = \frac{1}{2} [(P_X - \bar{A}_X)^2 + P_Y^2] + \frac{\varepsilon}{k} \sum_{i=1,2} \cos(\kappa X - \nu_i \tau) \quad (2.3.2)$$

where

$$\begin{aligned} H &= \frac{1}{m\omega_{c,i}^2 \bar{r}_L^2} h & \tau &= \omega_{c,i} t & \nu_i &= \frac{\omega_i}{\omega_{c,i}} & \kappa &= k \bar{r}_L & \varepsilon &= \frac{qE_0}{m\omega_{c,i}^2 \bar{r}_L} \\ X &= \frac{x}{\bar{r}_L} & Y &= \frac{y}{\bar{r}_L} & \bar{A}_X &= \frac{q}{m\omega_{c,i} \bar{r}_L} A_x(\bar{r}_L Y) & P_X &= X' + \bar{A}_X & P_Y &= Y' \end{aligned}$$

with the prime (') denoting differentiation with respect to  $\tau$ . The magnetic field configuration can also be normalized to

$$\mathbf{B}(Y) = B_0 \tanh \frac{3Y}{\bar{\delta}} \hat{\mathbf{z}} \quad (2.3.3)$$

where  $\bar{\delta} = \delta/\bar{r}_L$ . Gardineer employs this normalization scheme so that simulations may be carried out with unspecified ion temperature.

## 2.3.2 Unperturbed Dynamics ( $\varepsilon = 0$ )

### Trajectory Classification

Here we consider the motion of ions in the magnetic null topography without perturbation from beating waves (i.e.  $\varepsilon = 0$ ). Jorns and Choueiri qualitatively and quantitatively characterized all possible trajectories an ion can follow[12], which are explored here. They show that ion motion can be characterized by the sign of its canonical  $X$ -momentum  $P_X$ . Specifically, ions with  $P_X > 0$  exhibit motion exclusively in the  $+\hat{\mathbf{x}}$  direction, while those with  $P_X < 0$  exhibit  $\nabla B$  drift<sup>3</sup> ( $-\hat{\mathbf{x}}$ ), figure-8 trajectories ( $\pm\hat{\mathbf{x}}$ ), or Larmor precession<sup>4</sup> (no net motion). Furthermore they relate the physical parameters of the orbit to  $H$  and  $P_X$  by the following two equations:

$$H = \frac{1}{2} \rho^2 \quad (2.3.4)$$

---

<sup>3</sup> $\nabla B$  drift is motion of the ion's guiding center due to a magnetic field gradient.

<sup>4</sup>Larmor precession describes the trajectory of an ion orbiting around a fixed guiding center with little or no net motion.

$$Y_{GC} = -\frac{B}{|B|}[P_X - \bar{A}_X(\delta) - \delta] \quad (2.3.5)$$

where  $\rho$  is the  $\bar{r}_L$ -normalized Larmor radius of the ion with guiding center  $(X_{GC}, Y_{GC})$  and initial position  $(X, Y)$  in the uniform magnetic field region.

The motion of all ions with  $P_X > 0$  is called “linear betatron”<sup>5</sup> (LB), characterized by a guiding center on the opposite side of the null plane such that the ion completes less than half of one orbit before reversing polarity. As mentioned at the beginning of this section, the result is net movement in the  $+\hat{\mathbf{x}}$  direction. Increasing  $H$  results in a guiding center further into the opposite region (i.e. a larger radius of gyration as per equation 2.3.4) and thus faster and more linear  $+\hat{\mathbf{x}}$  motion. Figure 2.4 shows such trajectories.

For the case of  $P_X < 0$ , the ion trajectory depends on its initial energy  $H$ , with increasing  $H$  correlating to more tendency in the  $+\hat{\mathbf{x}}$  direction. Figure 2.5 shows this phenomenon. With low initial energy (a), ions will be trapped in Larmor precession within the uniform field region. If an ion enters the sloped region without crossing the null, it will experience a  $\nabla B$  drift in the  $-\hat{\mathbf{x}}$  direction (b). Once it slightly crosses the null, it will exhibit a figure-8 trajectory, completing more than half of one orbit on each side of the null plane. This path can result in  $-\hat{\mathbf{x}}$  movement for lower  $H$  (c) that tends more towards  $+\hat{\mathbf{x}}$  with increasing energy (d, e, f).

Figures 2.4 and 2.5 represent the range of trajectories an unperturbed ion may follow in our magnetic null field configuration. Figure 2.6 shows the occurrence of each of these paths at given initial  $H$  and  $P_X$  values.

## Design Implications

Jorns and Choueiri showed that there is indeed a net  $+\hat{\mathbf{x}}$  ion flow along the magnetic null for an unperturbed thermalized Maxwellian distribution of ions[12]. This current is produced by the field configuration converting a portion of the ions’ thermal energy to linear momentum. This implies that the exhaust velocity  $u_{ex}$  for a perfect magnetic null would be equal to the average ion velocity perpendicular to the field  $\bar{v}_\perp$ . However, due to the nature of the exiting ion trajectories about the null, simulations reveal that  $U_{ex} = 0.6$  (where  $U_{ex} = u_{ex}/\bar{v}_\perp$ )[10]. This corresponds to a specific impulse of just 40 s with Argon gas as propellant, ignoring ions that remain trapped or lost inside the thruster.

Although have the desirable result of a directed ion current, it is clear from the

---

<sup>5</sup>This borrows its name from the analogous “betatron orbits” defined in the Field-Reversed Configuration[15].

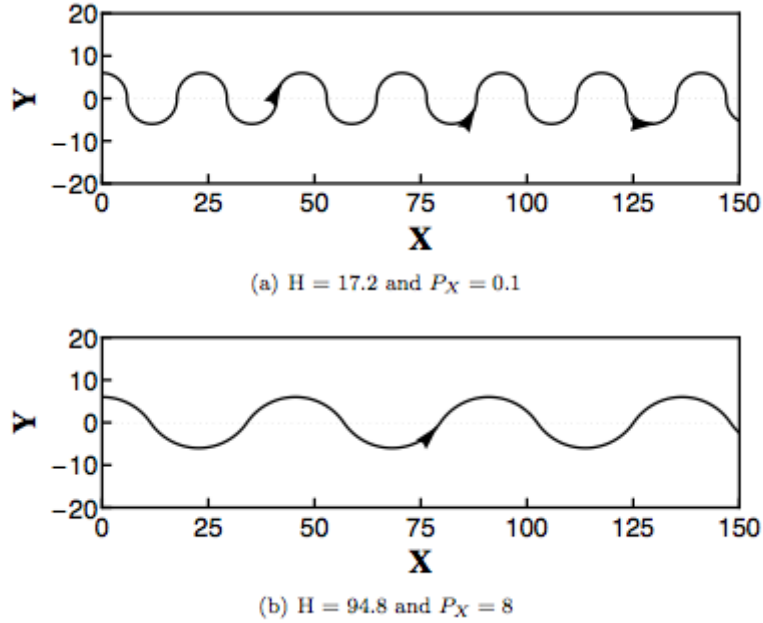


Figure 2.4: LB trajectories ( $P_X > 0$ ). Higher  $H$  results in a more linear path.[12]

above performance benchmarks that the flow must be considerably augmented for the MagNul to be a viable thruster option. Based on our intuitive understanding of thrust production in the MagNul, our goal is to increase both the number of ions crossing the null and the speed at which they travel<sup>6</sup>.

Gardineer derived a useful approximation for thrust density (thrust per unit depth in  $\hat{\mathbf{z}}$ )[10]:

$$\frac{T}{l} = \sqrt{32} L \xi_f U_{ex}^2 \frac{n_i \sqrt{m_i} (k_B T_i)^{3/2}}{q B_0} \quad (2.3.6)$$

where  $L$  is the thruster length in  $\hat{\mathbf{x}}$ ,  $\xi_f$  is the fraction of forward-drifting ions,  $n_i$  is the average ion density,  $m_i$  is the single ion mass,  $k_B$  is Boltzmann's constant, and  $T_i$  is the average ion temperature. Many of these parameters are constrained:  $m_i$ ,  $q$ ,  $n_i$  and  $L$  are fixed by the apparatus;  $\xi_f$  and  $U_{ex}$  depend intrinsically on the only parameters we may freely manipulate, which are  $T_i$  and  $B_0$ . Current augmentation amounts to increasing thrust density through the manipulation of these two parameters.

In the unperturbed case, ions cannot be heated, thus optimizing  $\frac{T}{l}$  depends solely on  $B_0$ . More specifically, it depends on  $\bar{\delta}$  (determined exclusively by  $B_0$  assuming a

---

<sup>6</sup>We may be tempted to simply raise the mass flow rate  $\dot{m}$  to achieve better performance benchmarks—this is not a feasible option. Aside from the engineering limitation on power required to ionize a greater mass flow, we would like to keep ion density  $n_i$  low so that  $\Omega_i$  remains high. From the ion dynamics explored thus far it is clear that cyclotron motion must be unimpeded by collisions for our understanding to hold true.

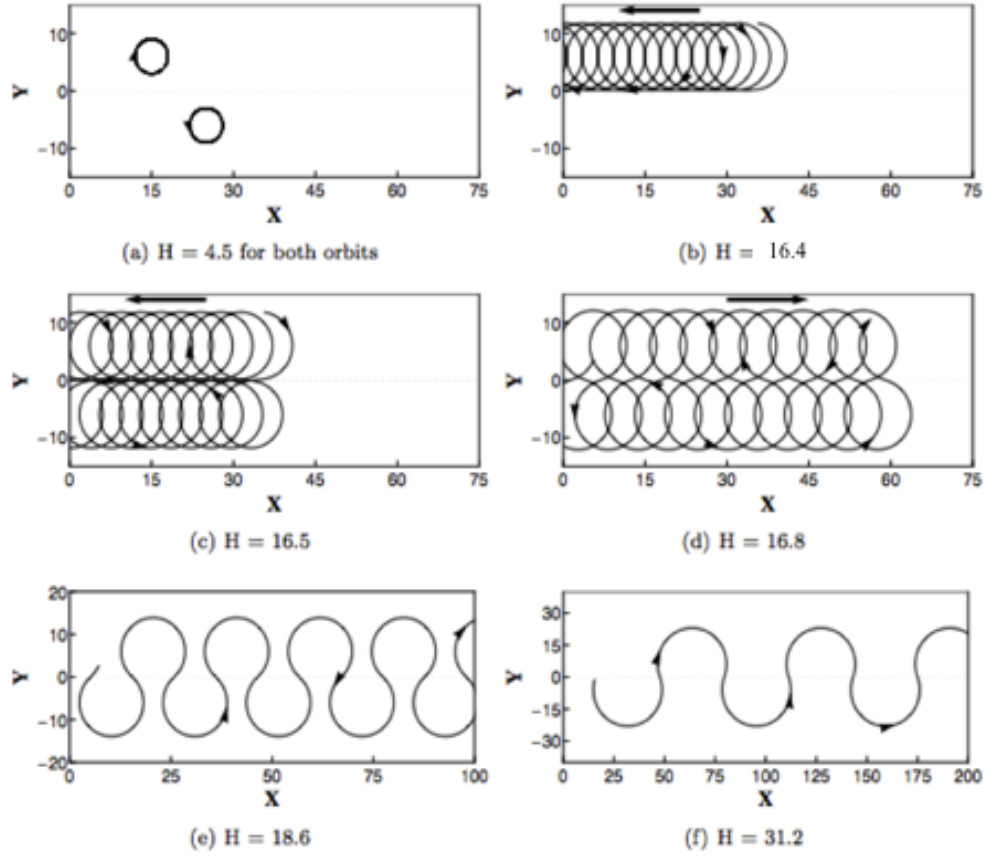


Figure 2.5: Trajectories for ions with  $P_X = -5.8$ . As  $H$  is increased, trajectories open up and approach LB.[12]

fixed  $\delta$ ); there exists a tradeoff between  $\rho$  being large enough relative to  $\bar{\delta}$  that the sloped region minimally alters the orbit shape as it passes through yet not so large that most ions are lost to the thruster walls, which exist at some distance  $|Y| = Y_{max}$ .

The only other method of raising thrust density is heating the ions. The energy of the ion is directly related to its Larmor radius by equation 2.3.4. Increasing temperature corresponds to increasing energy  $H$ , thereby extending the Larmor radius  $\rho$ . If  $\rho$  becomes large enough, the ion will enter a forward-drifting path (i.e. cross the null) and exit the thruster. We will denote a Larmor radius large enough to place an ion in a forward-drifting trajectory by  $\rho_f$  and define it as  $\rho_f \approx |Y_{GC}|$ . It is clear that increasing  $H$  translates to an increased number of thruster-exiting ions; this notion is supported by figure 2.6. The increased radius also corresponds to increased velocity via the equation[5]

$$\rho = \frac{m_i v_{\perp}}{|qB|} \quad (2.3.7)$$

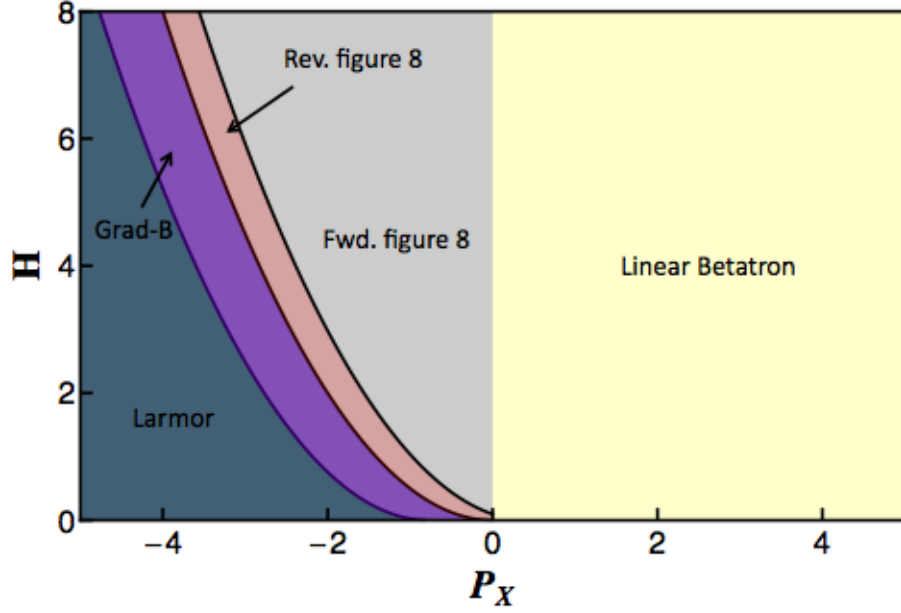


Figure 2.6: Trajectory classification of an ion based on its initial  $H$  and  $P_X$ . [12]

Increasing  $v_{\perp}$  will increase both the average exit velocity of the ion and the linearity of its trajectory, creating a more direct beam. With this picture of how to improve the thruster performance, it becomes desirable to energize the ions trapped in Larmor precession to forward-drifting trajectories using a short time-scale acceleration method. This energization will be achieved with BEW heating.

### 2.3.3 Perturbed Dynamics ( $\varepsilon > 0$ )

#### Acceleration Regimes

BEW heating may accelerate ions in a variety of ways. Gardineer et al [10] categorized the acceleration experienced by an ion into regimes defined by its initial gyroradius  $\rho_0$ . These three regimes are forbidden, regular, and stochastic acceleration and are defined as follows.

**Stochastic:** an ion undergoing stochastic acceleration receives large periodic “kicks” in energy from the BEW. These kicks serve to substantially and rapidly increase  $\rho$ , raising the probability that the particle will exit the thruster (by reaching  $\rho \geq \rho_f$ ). In fact, these stochastic kicks are so energetic it is a safe assumption that all ions that reach this regime exit the thruster (except in extreme cases discussed in chapter 4). The stochastic regime is defined by a threshold radius  $\rho_{th}$  above which this

type of acceleration occurs. The beating wave parameters determine this threshold by the relation

$$\rho_{th} = \frac{\nu}{\kappa} - \sqrt{\frac{\varepsilon}{\kappa}} \quad (2.3.8)$$

Furthermore, this acceleration produces an effect called “ion channeling” whereby  $Y_{GC}$  drifts in the  $\mathbf{k} \times \mathbf{B}$  direction, preferentially transporting ions toward the null plane. This is a useful side effect as it reduces wall losses, an appreciable source of energy loss in many electric propulsion devices.

**Regular:** for ions whose radii are not large enough to receive stochastic energy kicks, the acceleration experienced is coherent. That is,  $\rho$  steadily increases with no change in  $Y_{GC}$ . The criterion for this type of acceleration is  $\frac{\rho_{th}}{2} < \rho_0 < \rho_{th}$ . The steady increase in  $\rho$  means that ions in the regular regime will eventually enter the stochastic regime.

**Forbidden:** ions in the forbidden acceleration regime undergo the same coherent acceleration as those in the regular regime with one caveat: they will never enter the stochastic regime. Therefore, for the most part, these ions are trapped in the thruster (except those meeting  $\rho \geq \rho_f \approx |Y_{GC}|$ ). This regime is defined by an initial radius  $\rho_0 < \frac{\rho_{th}}{2}$ .

## Design Implications

Any ion in the regular or stochastic regimes may be considered forward-drifting<sup>7</sup>. It is evident then that maximizing the augmentation of the ion current (and thus the effectiveness of the BEW) amounts to maximizing the number of ions initially in these regimes. We cannot change the thermal distribution of the gas, described by the Maxwellian, thus we must optimize the acceleration threshold relative to the initial thermal ion radii. Since this is described by equation 2.3.8, the wave parameters must be optimized to achieve the minimum  $\rho_{th}$ .

Gardineer[10] performs the optimization, arriving at  $\varepsilon = 10$ ,  $\kappa \approx 0.16$ , and  $\nu \approx 1.47$ . This yields  $\rho_{th} = 0.75$ . This is a very good result; since the RMS radius is  $\rho = 1$ , the majority of ions have a  $\rho_0$  in the stochastic regime ( $\rho_0 > 0.75$ ) and very few are in the forbidden regime ( $\rho_0 < 0.375$ ). The fractions of ions initially in the stochastic, regular, and forbidden regimes are  $\xi_{st} = 0.64$ ,  $\xi_{reg} = 0.3$ , and  $\xi_{forb} = 0.06$  respectively, giving a total fraction of forward-drifting ions  $\xi_f = 0.94$ . In a thruster setting with walls at  $|Y_{max}| = 50$  and the optimized wave parameters, numerical

---

<sup>7</sup>Ignoring those lost to the thruster walls and excepting those in the forbidden regime with  $\rho \geq \rho_f$ .

simulation revealed the fraction of ions that exit is  $\xi_{ex} = 0.837$  with the remaining ions lost to the walls and virtually none trapped in Larmor precession. The  $I_{sp}$  using Argon gas at  $T_i = 0.1$  eV is roughly 1500 s[10].

These results represent a significant augmentation of the ion beam along the magnetic null. We have now described the MagNul as two distinct components working in tandem; the magnetic field topography serves to produce linear momentum while the BEW is a system by which this momentum production is enhanced.



# Chapter 3

## Proof-of-Concept MagNul Design

### 3.1 Design Criteria

In the previous chapter, we gained an understanding of the dynamics at play due to both the magnetic field topography and the beating wave mechanism comprising the MagNul. These drive the ultimate design of the device, which will take advantage of the intrinsic dynamics in such a way to most effectively and efficiently generate thrust. The primary criteria driving the design are summarized in this section.

#### 3.1.1 Uniform Field Region

There are two aspects of the uniform magnetic field region  $|Y| > \delta$  that must be considered: size and uniformity.

##### Size

This region should occupy as large a fraction of the thruster chamber as possible. We saw in section 2.3.3 that virtually no ions remained trapped in Larmor precession after BEW acceleration despite a significant fraction being trapped in the unperturbed case (see Figure 2.6). This implies that the uniform region acts as a reservoir from which Larmor-orbiting ions are accelerated into forward-drifting orbits and that virtually all such ions will achieve this. As such, the uniform region (in which ions exhibit Larmor precession) should be maximized.

## Uniformity

The region  $|Y| > \delta$  should be uniform enough that a Larmor-orbiting ion will not shift out of phase with the beating wave due to  $\nabla B$  drift, or at least remain in phase long enough to be accelerated to a forward-drifting orbit. In the mathematical construct defining the ideal magnetic topography (Figure 2.2),  $\nabla B \approx 0$  for  $|Y| > \delta$  thus we need not be concerned with drifting out of phase. However, in a physically constructed field configuration the uniform region will have small gradients, especially when approaching the sloped region. It becomes necessary then to define a maximum allowable drift velocity under which the field may be called uniform.

The drift velocity  $v_d$  due to a magnetic field gradient  $\nabla B$  is[5]

$$v_d = \frac{1}{2} r_L v_\perp \frac{\mathbf{B}(y) \times \nabla \mathbf{B}(y)}{B(y)^2} \quad (3.1.1)$$

Transforming to our  $\bar{r}_L$ -normalization scheme, this becomes

$$V_d = \frac{1}{2} \rho V_\perp \frac{\mathbf{B}(Y) \times \nabla \mathbf{B}(Y)}{B(Y)^2} \quad (3.1.2)$$

where  $V_d = v_d/\bar{v}_\perp$  and  $V_\perp = v_\perp/\bar{v}_\perp$ . Since  $\mathbf{B}$  is along  $\pm \hat{\mathbf{z}}$  and  $\nabla \mathbf{B}$  is along  $\pm \hat{\mathbf{y}}$ , the direction of this drift will be in  $\pm \hat{\mathbf{x}}$  (parallel to the wave direction  $\mathbf{k}$ ).

We approximate an ion as having shifted out of phase once its guiding center has drifted half of the wavelength of the beating wave, or  $\frac{1}{2}\nu$ . For the optimized wave parameters given in section 2.3.3, this corresponds to a shift of  $X = \pm 0.735$ . Further, we conservatively estimate based on single-ion simulations[9] that no ion will take longer than  $\tau_{max} = 10$  to be accelerated to a forward-drifting path. Thus the maximum allowable drift velocity at a given point for it to be considered uniform is

$$|V_{d,max}| = \frac{\nu/2}{\tau_{max}} = \frac{0.735}{10} = 0.0735 \quad (3.1.3)$$

In physical terms, this means that an ion with a gyroradius  $\rho$  must drift less than  $0.0735\rho$  per orbit it completes in order to be considered inside the region of uniformity. Again, this is a conservative estimate; many if not most ions simulated reached  $\rho > \rho_f$  within  $\tau = 2$ , yet we set  $\tau_{max} = 10$  so that all ions are encompassed. We will use criterion 3.1.3 later to quantify the size of the uniform field region and  $\delta$ .

### 3.1.2 Magnetic Reversal Width

The space over which the polarity reversal occurs  $|Y| \leq \bar{\delta}$  should be as small as possible with one caveat regarding electron dynamics. As mentioned in section 2.3.2, this is so that the path of an ion crossing the reversal is minimally affected by the steep gradient. However, the null half-width should be large relative to the electron thermal Larmor radii  $\rho_{e,th}$  so that electrons experience  $\nabla B$  drift out of the thruster.

Feldman[7] showed that to ensure both ions and electrons exhibit predominately forward-drifting orbits, the following criterion must be met:

$$\rho_{e,th} \ll \bar{\delta} < \rho_i \quad (3.1.4)$$

Note that  $\rho_i$  is the post-energization ion radius. Electrons are governed by the same equations of motion as ions but with opposite polarity and much smaller characteristic gyroradii. As a result, their LB and figure-8 orbits are in  $-\hat{\mathbf{x}}$  and  $\nabla B$ -drift trajectories are in  $+\hat{\mathbf{x}}$ , the opposite of the case for ions. The criterion  $\rho_{e,th} \ll \bar{\delta}$  arises from the desire to maximize  $\nabla B$ -drifting orbits for electrons, maintaining quasi-neutrality in the thruster by having ions and electrons exiting at roughly the same rate. Indeed, Feldman shows that electrons exit the thruster at a similar rate and velocity as ions, affirming the feasibility of the MagNul from a charge neutrality standpoint.

In practice, we need only design for the criterion  $\bar{\delta} < \rho_i$ ; it is virtually impossible in a physical electromagnetic coil system to achieve a magnetic reversal region near the order of  $\rho_{e,th}$  without reducing the thruster itself to that size (fractions of a millimeter), so we attempt to generate the smallest  $\delta$  possible without regard for electron orbits.

## 3.2 Design of Coils

### 3.2.1 Coil System

Using the above design criteria as a guide in combination with the physical constraints of the vacuum chamber and test stand, we construct a system of electromagnetic coils to generate the best achievable field topography. We naturally gravitate towards Helmholtz coils or a Helmholtz-like geometry given the need for field uniformity. The main chamber area should thus resemble two Helmholtz-like coil configurations atop one another with opposing field directions.

The design finally arrived at is seen in Figure 3.1. The thruster chamber itself lies between the middle two sets of coils. Each pair of coils is rectangular in shape and has a Helmholtz spacing such that the distance between the center of each coil in  $\hat{\mathbf{z}}$  is equal to the height of each coil in  $\hat{\mathbf{y}}$  (Figure 3.2).

One major problem discovered during the design process was that with just two pairs of Helmholtz coils, there was twice as much current running near the null plane at  $Y = 0$  as there was at the top and bottom edges of the system, meaning the field generation was twice as strong at the  $Y$ -center as at the edges. This led to a linear field gradient from  $Y = 0$  to  $Y = \pm Y_{max}$ , eliminating the uniform region. To alleviate this, the current had to be doubled at the upper and lower edges of the main coils. This required adding a pair of coils above and below the main two pairs so that the effect experienced at the null plane  $Y = 0$  (i.e. the effect of one coil's field generation on the other's) is mimicked at the outer ends of the main coils  $Y = \pm Y_{max}$ .

The choice of a rectangular design was simply so that the coils are very close (making the null region very thin) for as much of the thruster as possible. Because the two rectangular coil pairs sit flush atop one another, the best possible magnetic null topography is generated for almost the entire length of the rectangle, excepting the  $X$ -boundaries where the vertical currents affect the field. The rectangles may be arbitrarily long in  $\hat{\mathbf{x}}$  and will generate the magnetic null topography for that entire length; the length settled on here was determined by the available space on the test stand.

The two main pairs of coils are wrapped around blocks of ferrite (the gray material in Figures 3.1 and 3.2). Ferrite is a ferrimagnetic ceramic that can help to enhance the strength and uniformity of a magnetic field passing through it. This enhancement scales linearly with the strength of the field passing through up to a certain saturation limit; the fields we will operate at are not strong enough to reach this limit[8]. In section 3.2.3, we will see the difference in field quality made by using ferrite.

The device as it will be oriented on the test stand is seen in Figure 3.2. The total length in  $\hat{\mathbf{y}}$  is 24 cm; this means  $y_{max} = 6$  cm and the thruster chamber itself is 12 cm. The total length in  $\hat{\mathbf{x}}$  is 12 cm. The total width in  $\hat{\mathbf{z}}$  is 6.5 cm; the coils themselves are each 2 cm thick with 2.5 cm of free space between them.

### 3.2.2 Construction of Coil System

The two main coil pairs were wound around blocks of FerroxCube 3C97 ferrite while the two secondary pairs were wound around aluminum blocks. All eight blocks

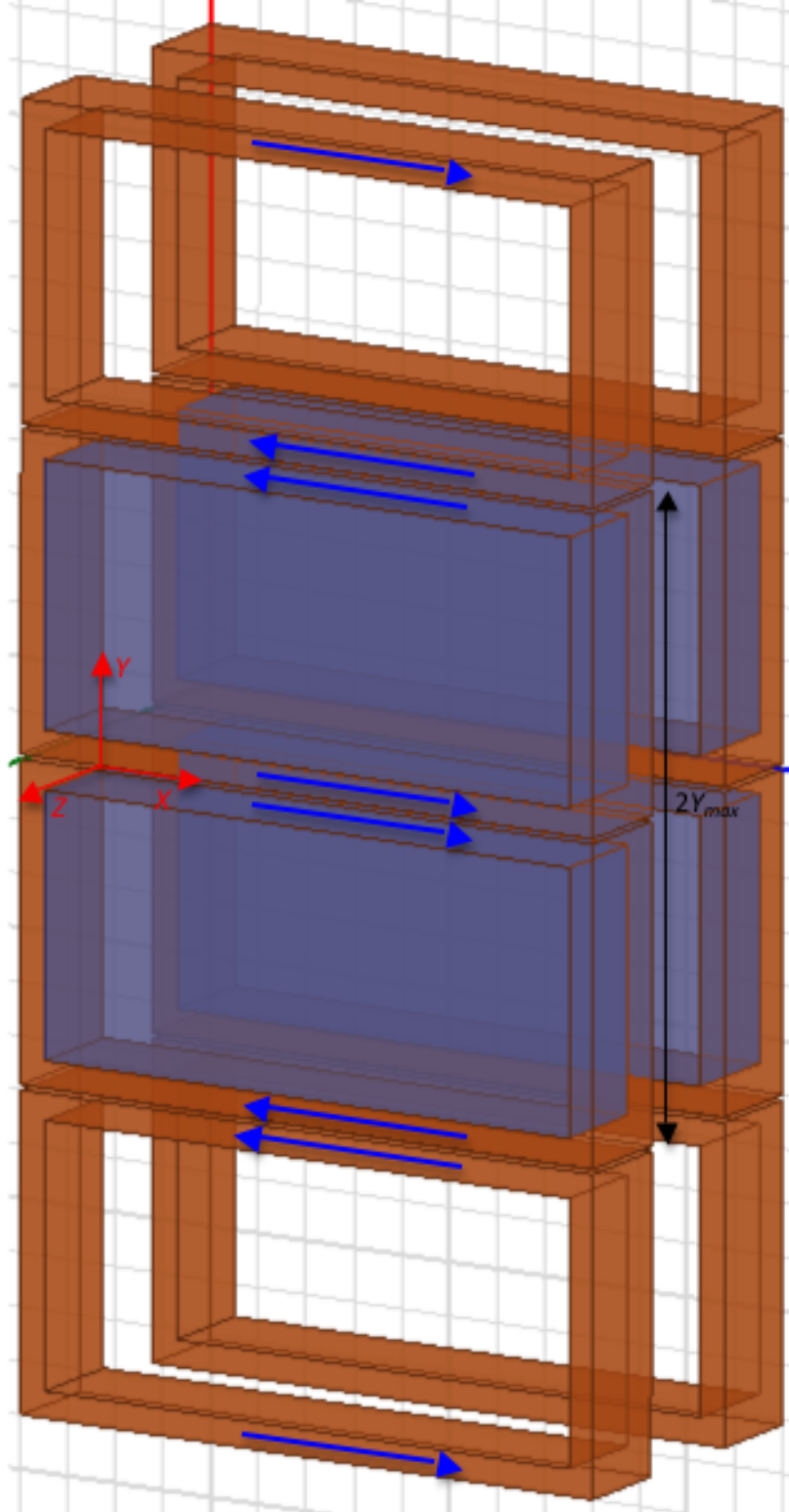


Figure 3.1: Electromagnetic coil system for generating magnetic null topography. Current direction is indicated by blue lines.

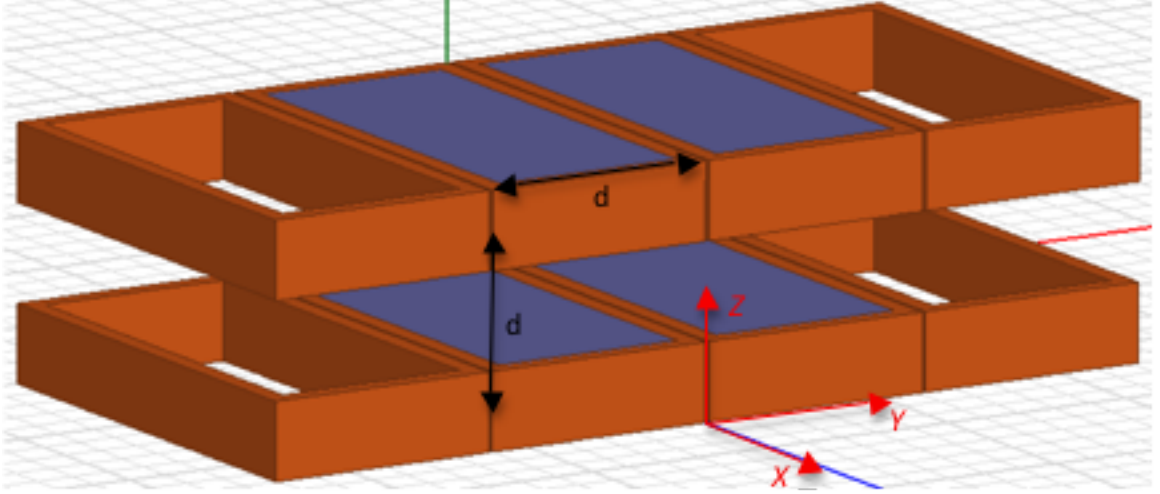


Figure 3.2: Electromagnetic coil system in the position it sits on the test stand.

have  $xyz$  dimensions of 108.7 mm  $\times$  48.7 mm  $\times$  20 mm with 1/8" radius rounded corners. The wire used was insulated copper 13 gauge square magnet wire. The insulation is rated for 200 °C; the rated ampacity at this temperature of 13 gauge wire far exceeds 20 A, which is around the maximum current we expect to require in this experiment. Each coil consists of 40 turns.

All eight coils are wired in series. As can be seen in Figure 3.3, the opposing sets of coils are each sandwiched between aluminum plates. The correct spacing and height of the device is achieved with standoffs cut from G10/FR4 Garolite.

### 3.2.3 Magnetic Field Generated

The magnetic field it generates in the thruster chamber section is seen in Figure 3.4. This magnitude plot was created in simulations using ANSYS Maxwell 3D finite element analysis software. The measured normalized field as a function of  $y$  can be seen in Figure 3.5. Measurements were taken with a Gaussmeter.

Using our criteria for uniformity, we can characterize the half-width of the null region  $\bar{\delta}$  and the size of the uniform region. Figure 3.6 shows the characteristic drift velocity as a function of  $Y$  for an ion with  $\rho = 1$ . The regions of uniformity are represented by values of  $Y$  where  $V_d < V_{d,max}$ . These regions occupy 40% of the thruster. From this plot we can also see that  $\delta \approx 1.5$  cm. Without ferrite,  $\delta \approx 2$  cm, a difference made apparent in Figure 3.7. Clearly the ferrite succeeded in significantly reducing the magnetic reversal width (25% reduction). Had we used ferrite in the

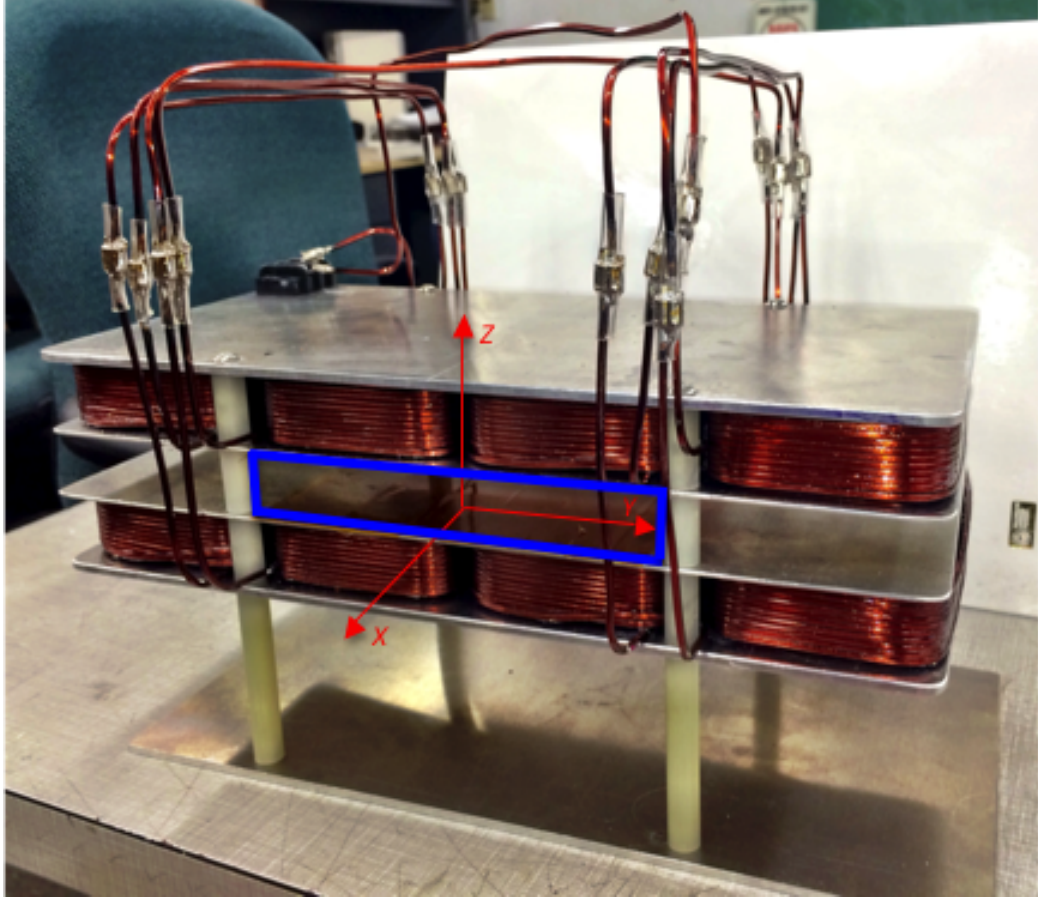


Figure 3.3: Device to generate the magnetic null field topography. The blue box outlines the exit of the thruster chamber region.

secondary coil pairs on top and bottom, the uniform region may also have been extended by  $0.5 \text{ cm}$  in  $\pm \hat{y}$ ; due to cost constraints this was not feasible.

The actual measured strength of the uniform regions  $B_0$  is  $16 \text{ Gauss/Amp}$ . As discussed in section 3.1.2, changing the field strength changes the ion gyroradius. Because  $\bar{\delta}$  is an  $\bar{r}_L$ -normalized parameter and  $\delta$  is a fixed number ( $1.5 \text{ cm}$ ), changing the magnetization will change  $\bar{\delta}$ . This relationship is shown for Argon gas at  $T_i = 0.1 \text{ eV}$  in Figure 3.8.

The design may be scaled linearly to any size so long as the crucial spacing relationships are maintained (i.e. Helmholtz-like geometry). The size of the magnetic reversal region remains a constant  $1.5 \text{ cm}$  no matter the device size. In this way, one may achieve a much larger relative uniform region by simply increasing the size of the device. The field remains highly uniform throughout the entire width between the coils.

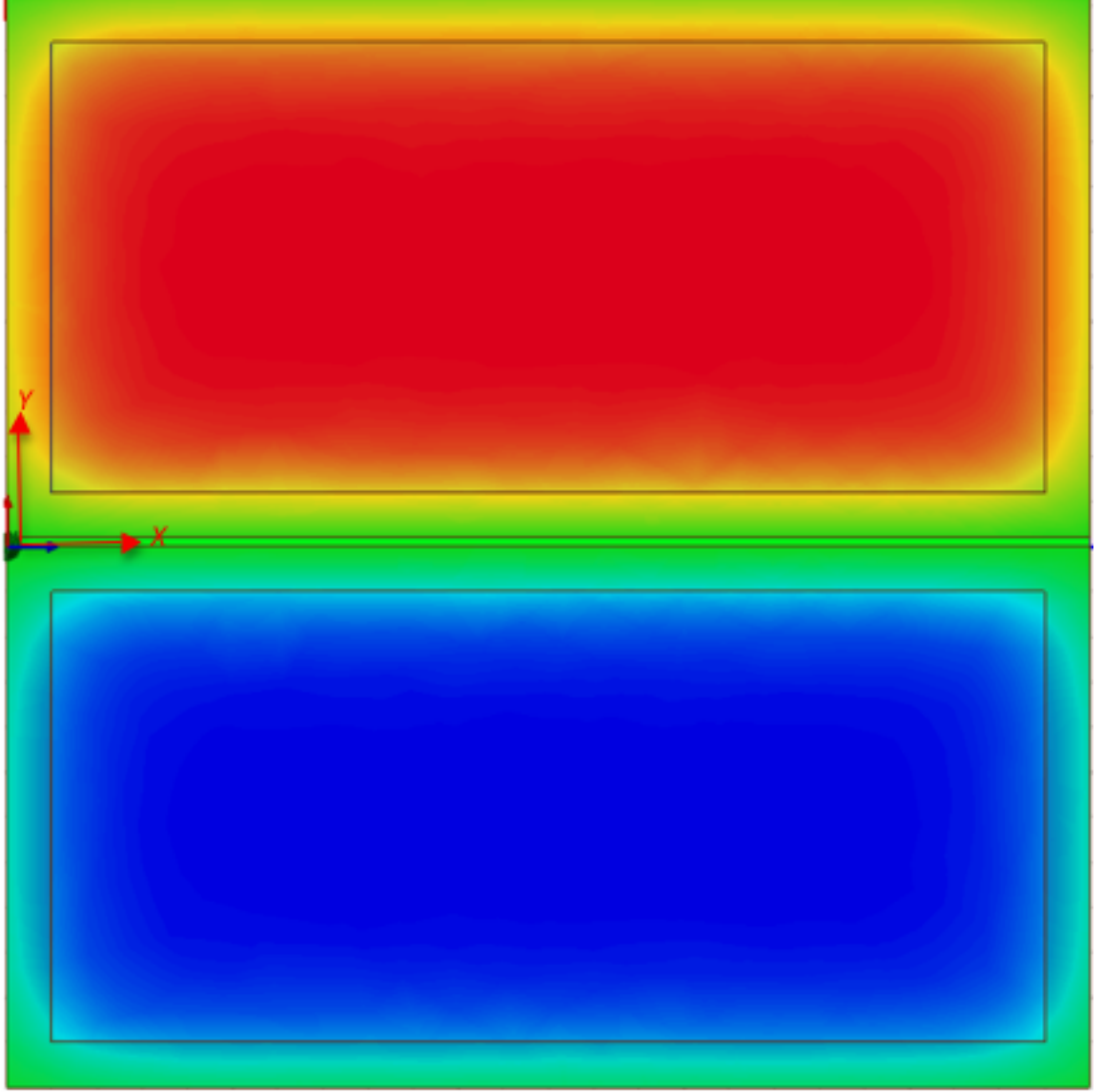


Figure 3.4: Magnetic field generated between the middle two pairs of coils (the thruster chamber). The outlined borders represent the shape of the coils. The red uniform region field lines point in  $+\hat{z}$  while the blue points in  $-\hat{z}$ . Green is a field strength of 0. (The color scale has been omitted intentionally since it included arbitrary field strength values).

### 3.3 Thruster Chamber

The MagNul was tested in a previously existing experimental setup; this not only limited the spacing of the coils, but also the chamber shape. The plasma injection scheme is configured to inject gas and generate a plasma inside a cylindrical chamber whose diameter is 8 cm (more information on this experimental setup can be found



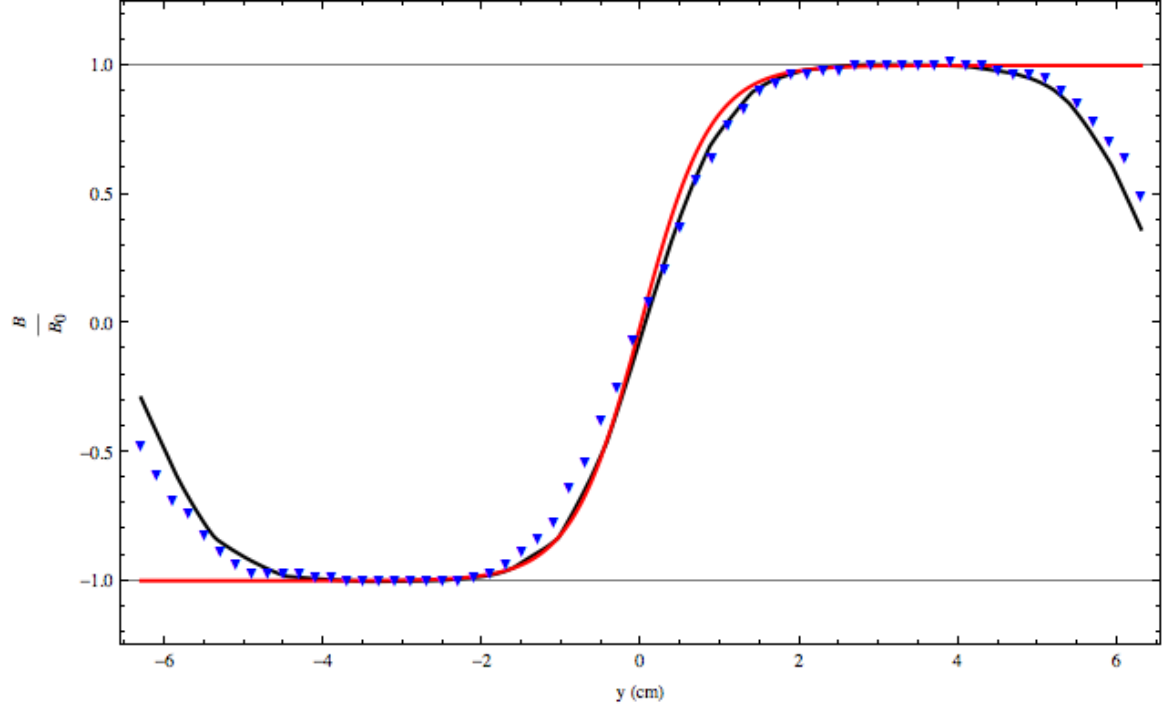


Figure 3.5: Comparison of the theoretical magnetic null topography with  $\delta = 1.5$  cm and  $\sigma = 1.72$  (red), the topography generated by the coil system in simulations (black), and the field generated by the physical coil system (blue).

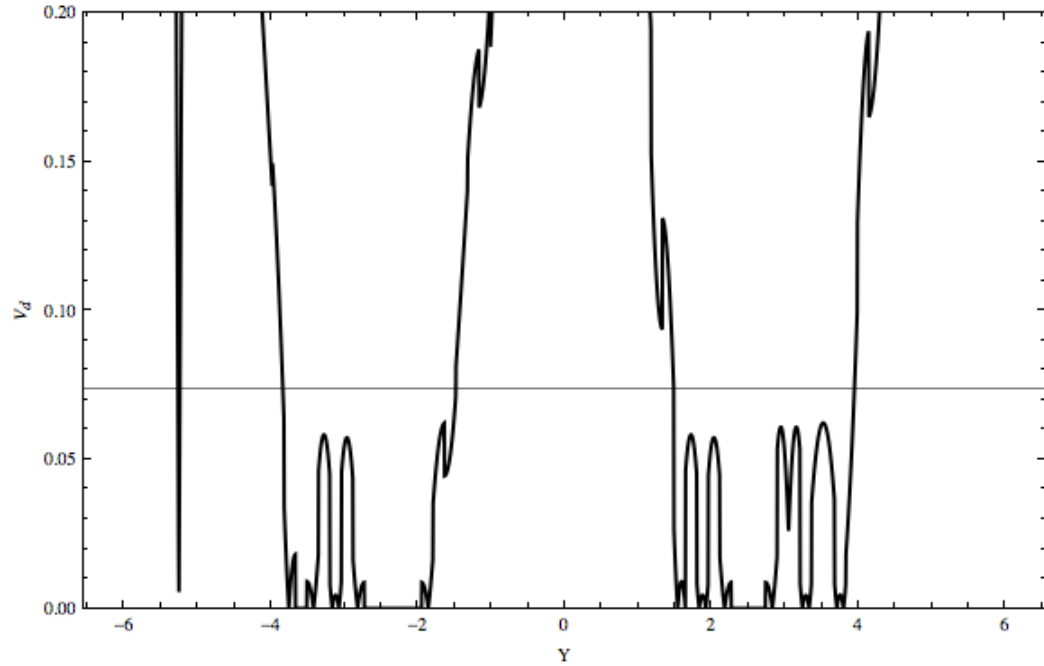


Figure 3.6: Magnitude of drift velocity  $V_d$  in  $\hat{\mathbf{x}}$  for  $\bar{r}_L = 1$  cm. The gray line represents  $V_{d,max}$ ; the regions in  $Y$  below this line are the uniform regions.

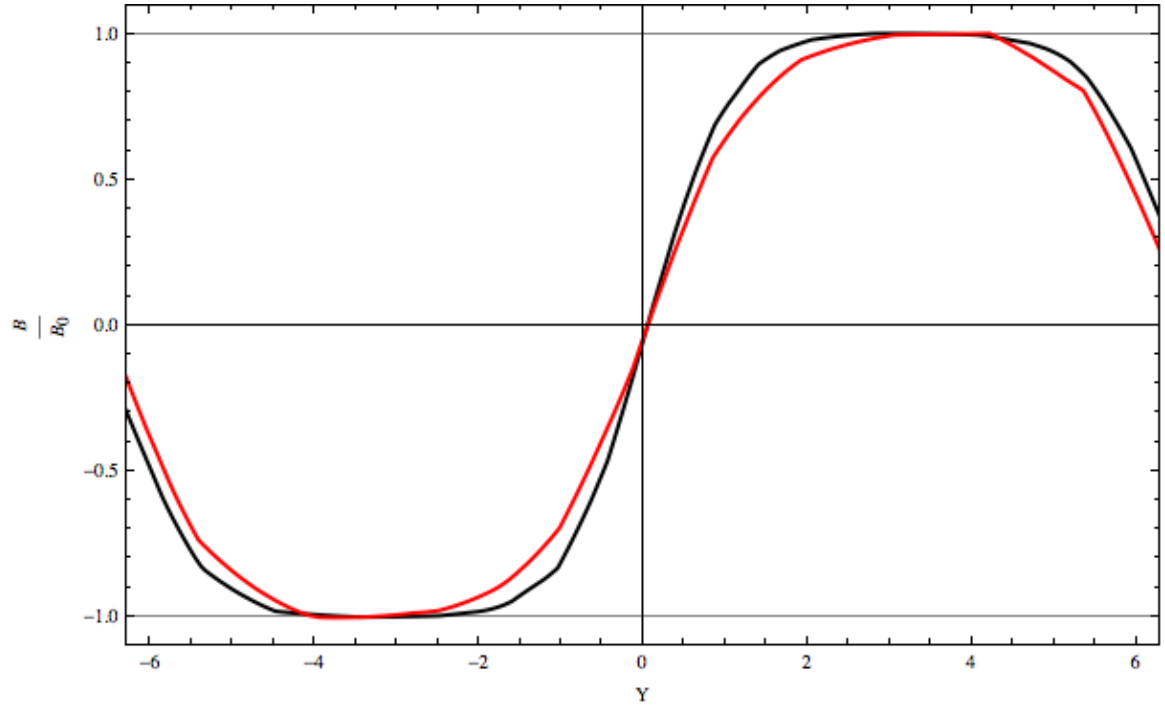


Figure 3.7: Comparison of the magnetic field generated when using ferrite in the main two coil pairs (black) and the field generated without ferrite (red).

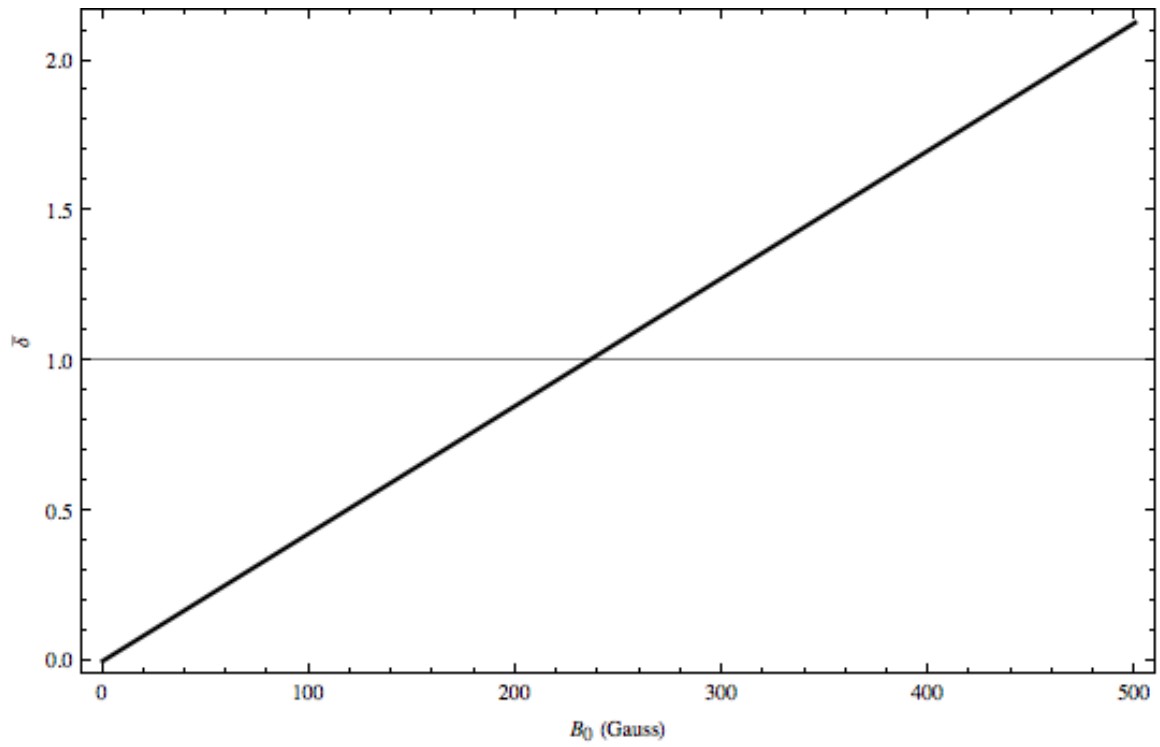


Figure 3.8: Relationship between  $\bar{\delta}$  and  $B_0$ . For  $\bar{\delta} = 1$ ,  $B_0 = 240$  Gauss.

in [16]). Due to the shape of the MagNul coil system, a rectangular tube is the only shape that fully encloses the usable magnetic field region. For these reasons, the chamber constructed for the MagNul consists of a cylindrical injection section, a rectangular section inside the coils, and a swept blend adapter section connecting the two. This was made as one single piece of borosilicate glass. The whole piece is configured coaxially with  $\hat{\mathbf{x}}$ . The cylindrical plasma generation section is 3 cm, the adapter is 3 cm, and the thruster chamber section is 12 cm (the  $x$ -length of the coils). The inner width of the thruster section is 1.2 cm (in  $\hat{\mathbf{z}}$ ) and its height is 12 cm (in  $\hat{\mathbf{y}}$ ). The chamber is shown in Figure 3.9.

Due to the nature of the chamber and the injection scheme, the thermal motion of the plasma will cause much of it to be lost to the walls. In fact, the only plasma expected not to be lost is that inside a fan originating at the injection hole and expanding to the rectangular opening at the exit of the thruster. This leads to over 99% of the plasma being lost to the walls<sup>1</sup>, the calculation of which is in Appendix A.

Since our understanding of the thruster dynamics is based on no electric field effects, it is useful to estimate the plasma sheath inside the chamber in order to know the amount of shielded volume that may be utilized. The sheath size is simply the Debye length  $\lambda_D$ [5]:

$$\lambda_D = \sqrt{\frac{\epsilon_0 k_B T_e}{n e^2}} = 7430 \sqrt{\frac{k_B T_e}{n}} \text{ meters} \quad (3.3.1)$$

where  $k_B T_e$  is the electron temperature in eV and  $n$  is the particle number density. In this experiment,  $k_B T_e \approx 6$  eV and  $n \approx 10^{16} - 10^{18} \text{ m}^{-3}$ . We calculated earlier that we will lose 99% of the plasma to the walls, reducing  $n$  by a factor of 100 to between  $10^{14}$  and  $10^{16} \text{ m}^{-3}$ . This gives a sheath size between 0.2 and 2 mm. The chamber width is 12 mm, so between 70% and 97% is shielded from wall potential effects.

These losses are detrimental for obvious reasons, mainly that they reduce the amount of plasma exiting the thruster and therefore the thrust generated. However, there may be some benefit from a density reduction in that it keeps  $\Omega_i$  high by reducing collision frequency. Additionally, the sheath limits the usable space of the chamber to the most uniform region, the area near the center plane.

---

<sup>1</sup>Later, we will add magnetic confinement to the chamber to alleviate some of these wall losses.

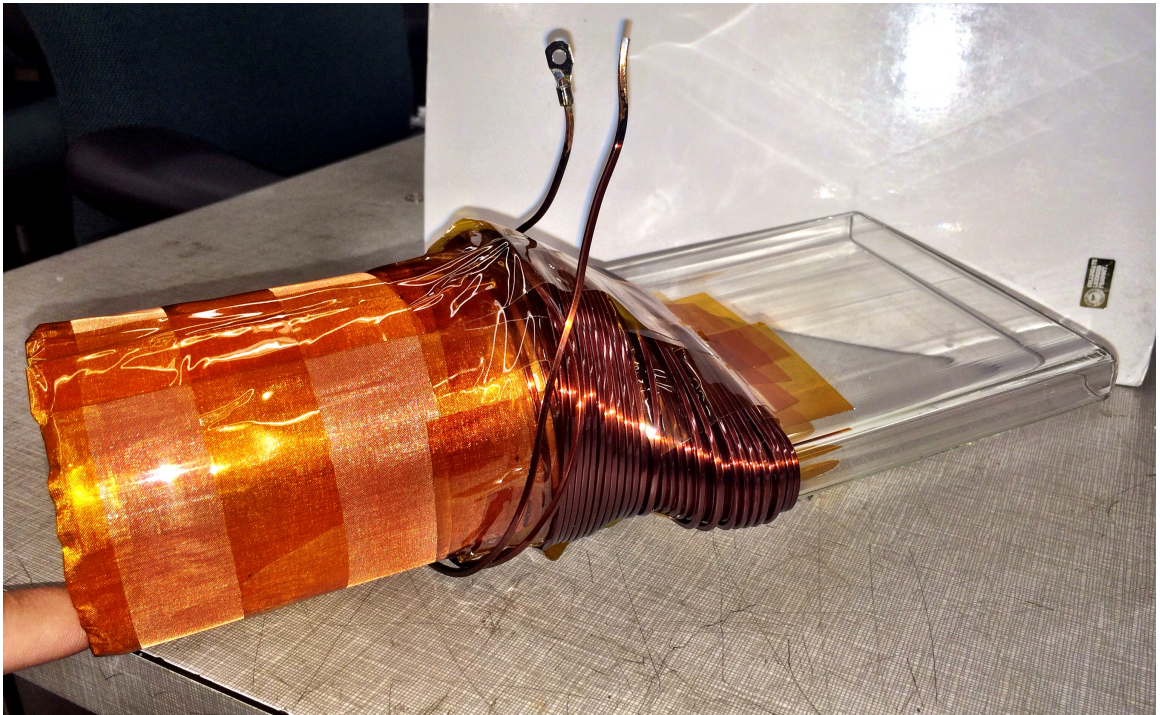


Figure 3.9: Glass chamber constructed for this experiment with its characteristic “duck-billed” shape. It is covered in a copper mesh to prevent stray RF outside the plasma source, which will be inside the cylindrical region as close to the swept blend as possible. In this image, the blended adapter section is wound with extra coils to magnetically confine the plasma; this will be discussed in Chapter 4.

# Chapter 4

## Results and Discussion

### 4.1 Revised Mathematical Construct

With the definition of uniformity given in section 3.1.1, we can mathematically represent the magnetic null topography with higher fidelity than equation 2.3.3. That construct, introduced by Jorns[12], applies a somewhat arbitrary scaling factor of 3 such that the curve “appears” uniform at  $y = \delta$  with no actual quantification. Now that we have a firm definition of what constitutes uniformity and non-uniformity in the magnetic field, we may revamp this description with a new scaling parameter,  $\sigma$ . The theoretical  $B_0$ -normalized null topography then is described as

$$\mathbf{B}(Y) = \tanh \frac{\sigma Y}{\bar{\delta}} \hat{\mathbf{z}} \quad (4.1.1)$$

With the correct  $\sigma$ , we can mathematically define a magnetic field with  $\bar{\delta}$  faithful to our definition of uniformity instead of the arbitrary visual approximation previously used. Since our definition of uniformity depends on the  $\nabla B$  ion drift velocity  $V_d$  at a given point, we expect  $\sigma$  (which determines the starting point of the uniform region) to have the same dependence. Further, since  $\sigma$  is a scaling parameter that allows us to decide exactly where the uniform region begins, we expect it to depend on the desired  $\bar{\delta}$  of the theoretical topography.

The derivation of  $\sigma$  can be found in Appendix B. We arrive at an implicit definition of

$$\frac{\nu \bar{\delta}}{2\tau_{max}} = \sigma \text{csch}(2\sigma) \quad (4.1.2)$$

This does still leave some arbitration in defining  $\tau_{max}$ ; for strong waves ( $\varepsilon \sim 10$ ),  $\tau_{max} = 10$  is perfectly reasonable, but for weaker waves this must be relaxed as it will take longer to accelerate an ion to a forward-drifting orbit. Additionally, if one takes a less conservative definition of uniformity then  $\tau_{max}$  may be much lower.

Suppose we wish to faithfully recreate the field measured in our constructed device. Plugging in  $\bar{\delta} = 1.5$  (assuming  $\bar{r}_L = 1$  cm so that  $y = Y$ ) and  $V_{d,max} = 0.0735$  as before, equation 4.1.2 is numerically solved to yield  $\sigma = 1.721$ . These conditions perfectly match those measured in the actual device, resulting in a perfect match of the point at which the uniform region begins; this is seen in Figure 4.1.

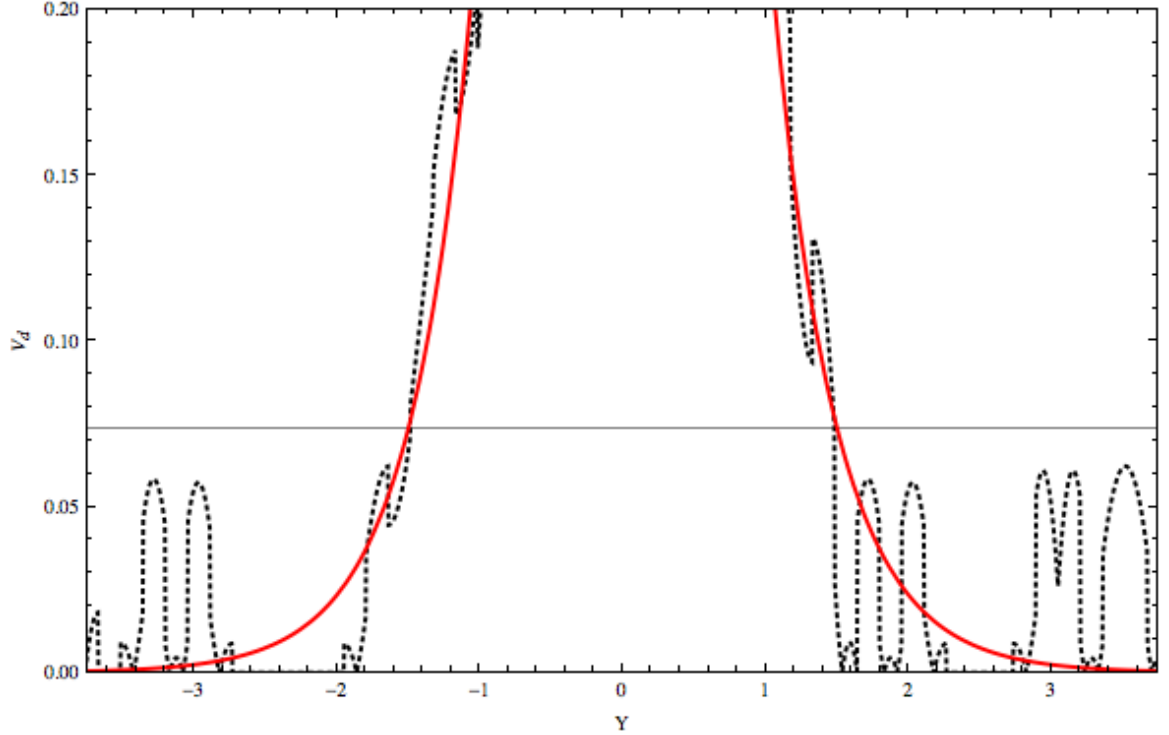


Figure 4.1: Comparison of the  $\nabla B$  drift in the actual device (black) and the theoretical reconstruction of the device (red). The gray line marks  $V_{d,max}$ . The region of uniformity begins at exactly the same  $Y$  for both the generated field and its mathematical reconstruction.

## 4.2 Magnetization and Performance

In section 2.3.2 we introduced the notion that operating at the correct  $B_0$ , and therefore  $\bar{\delta}$ , could enhance the performance of the thruster. Performance suffers when ions are either lost to the walls or exit the thruster before being accelerated.

Because the uniform Larmor region acts as a reservoir from which to accelerate ions to high-speed forward-drifting trajectories, it is logical that the fraction  $\xi_{tr}$  of pre-BEW heating ions trapped in these Larmor orbits should be maximized, thereby reducing the fraction lost to the walls  $\xi_{lost}$  and the fraction exiting the device  $\xi_{ex}$  before receiving BEW energy. Once the heating is applied, virtually all trapped ions will become thruster-exiting ions but with high velocity  $u_{ex}$ .

#### 4.2.1 Performance Simulations

To achieve a high  $\xi_{tr}$  before applying BEW heating, a strong magnetic field should be applied to keep the gyroradii small. Since any ion with  $|Y_{GC}| + \rho \geq |Y_{max}|$  will be lost to the walls, reducing the size of  $\rho$  simultaneously reduces  $\xi_{lost}$  and increases  $\xi_{tr}$ . Here we show this effect through simulation.

Monte Carlo simulations were conducted, each of 2500 ions with initial positions evenly distributed across a two dimensional plane representing the center plane of the chamber and initial velocities sampled from the 2D Maxwellian. The single ion dynamics were recreated for each ion, ignoring collisions and electronic effects, in a magnetic field described by the actual measured field at this plane in the real device. The final state of the ion was recorded: if it left the thruster and at what velocity; if it hit a wall; or if it remained trapped. Between simulations,  $\varepsilon$  and  $B_0$  were varied to show pre- and post-heating thruster conditions at different initial  $\bar{r}_L$ . The optimized wave parameters were used in every perturbed case. This procedure closely matched that taken by Gardineer[10] so that comparison to those results is valid.

Results of some simulations are shown in Table 4.1. They confirm the assertion that smaller initial orbit size leads to a significant reduction in wall losses; comparing Figures 4.2 and 4.3 this is immediately obvious. In the case where the initial gyroradius is a larger fraction of the thruster (low magnetization), all ions are lost except those near the exit due to the stochastic energy kicks (and therefore radius jumps as per equation 2.3.4) pushing their orbits out to the walls. The higher magnetization (tighter orbits) leads to an increase in the unperturbed  $\xi_{tr}$  from 0.27 to 0.716, enabling a substantially larger portion of the particles to be subjected to BEW acceleration. The benefit of this effect is evidenced by the more than tenfold increase in  $I_{sp}$  between the perturbed low and high magnetization cases, a function of both  $U_{ex}$  and  $\xi_{ex}$ .

	Unperturbed	Perturbed
Low Magnetization $Y_{max} = 3$ $B_0 = 176$ Gauss	$\xi_{tr} = 0.27$ $\xi_{lost} = 0.345$ $\xi_{ex} = 0.385$	$\xi_{tr} = 0$ $\xi_{lost} = 0.757$ $\xi_{ex} = 0.243$ $U_{ex} = 2.94$ $I_{sp} = 50$ s
High Magnetization $Y_{max} = 12$ $B_0 = 705$ Gauss	$\xi_{tr} = 0.716$ $\xi_{lost} = 0.13$ $\xi_{ex} = 0.154$	$\xi_{tr} = 0$ $\xi_{lost} = 0.329$ $\xi_{ex} = 0.671$ $U_{ex} = 14.1$ $I_{sp} = 670$ s
Ultra-High Magnetization $Y_{max} = 120$ $B_0 = 7050$ Gauss	$\xi_{tr} = 0.935$ $\xi_{lost} = 0.042$ $\xi_{ex} = 0.023$	$\xi_{tr} = 0.190$ $\xi_{lost} = 0.150$ $\xi_{ex} = 0.660$ $U_{ex} = 20.6$ $I_{sp} = 960$ s

Table 4.1: Monte Carlo numerical simulation results for varying levels of magnetization.

### 4.2.2 Implications

The simulations conducted for performance prediction in the physically constructed field and chamber geometry confirm our hypothesis that reducing initial orbit sizes by strengthening  $B_0$  leads to an improved ion current. Specifically this is achieved by reducing the fraction of ions lost to the wall and allowing for more LB trajectories, increasing both  $\xi_{ex}$  and  $U_{ex}$ . However, there is an apparent upper bound on the benefit gained from strengthening the magnetic field; as  $\bar{r}_L$  gets smaller, the BEW are unable to increase some ions' radii enough that they can enter forward-drifting trajectories. This causes ions to be trapped even after heating is applied, as can be seen in the ultra-high magnetization case of Table 4.1. Looking at Figure 4.4, we see that  $\xi_{ex}$  begins to decrease just as  $\xi_{tr}$  departs from 0, supporting this notion. At even higher field strengths ( $B_0 = 70500$  Gauss,  $\bar{\delta} = 300$ ), the post-heating fraction of trapped ions climbs to  $\xi_{tr} = 0.9$  and the magnetization effect drops off enough to reduce the  $I_{sp}$  to just 60 s.

This implies that there is some ideal level of magnetization for this thruster geometry where both the pre-acceleration trapping of ions and the effectiveness of the BEW are maximized. One could measure this in an experimental setting by taking measurements of the velocity distribution of ions in the thruster plume at varying operational field strengths. We should expect to see increasing performance as  $B_0$  is increased up to a certain point after which it drops off. Preliminary evidence of this



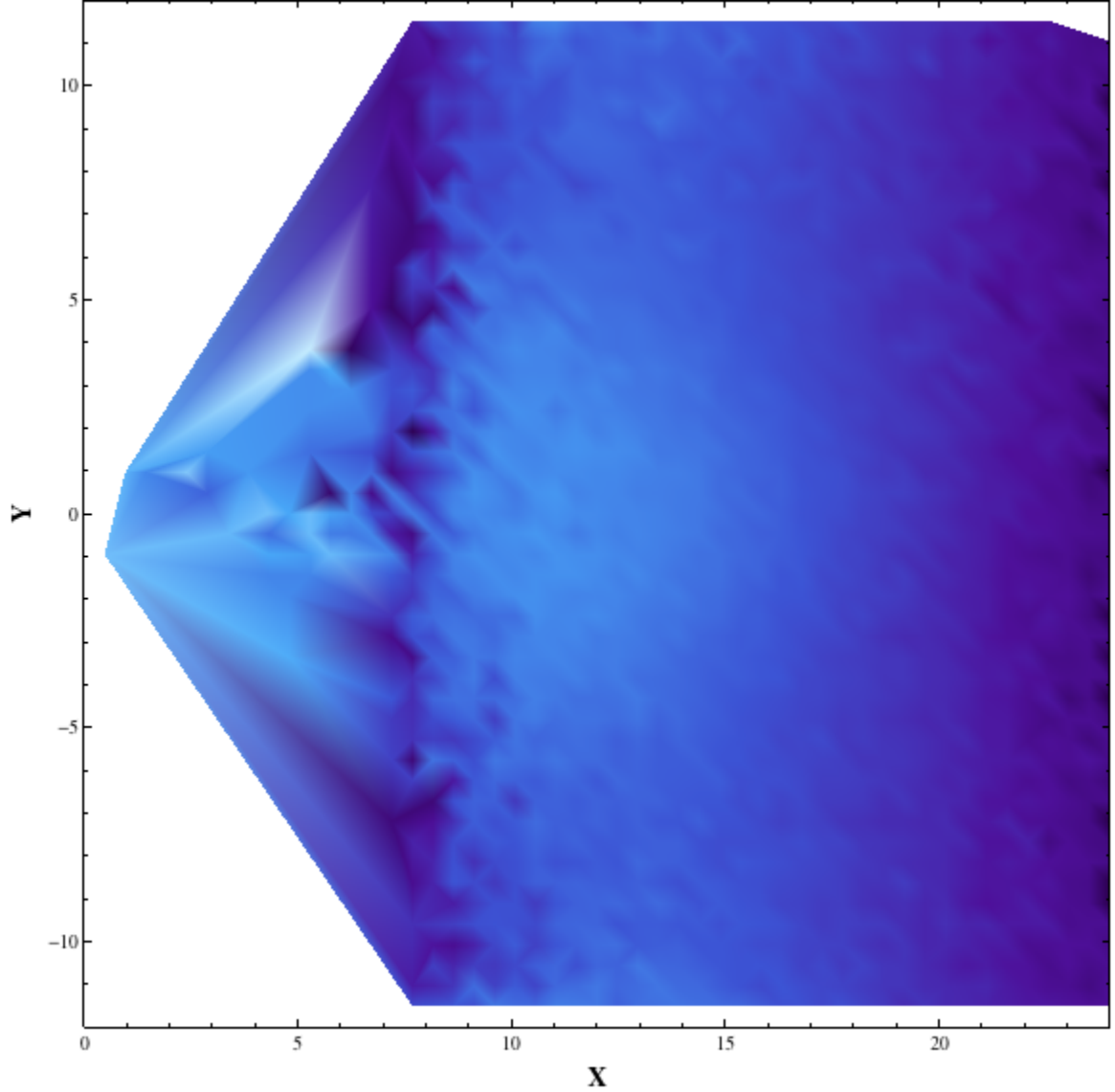


Figure 4.2: Color map of the eventual exit velocity of an ion as a function of its initial position  $(X, Y)$  in the heated, high magnetization case ( $B_0 = 705$  Gauss,  $\bar{\delta} = 3$ ). Lighter blue represents higher exit velocity. Empty white space represents ions that have been lost to the walls.  $\varepsilon = 10$ ,  $\kappa = 0.16$ ,  $\nu = 1.47$ .

phenomenon is seen in Figure 4.5. Due to computational limitations on simulation run time, only a few data points are calculated; however, this is an example of the type of metric we wish to quantify in an experimental setting for the MagNul.

The peak in  $I_{sp}$  is directly related to the peak in  $\xi_{ex}$ . The  $u_{ex}$  computed by our simulations is the average exit velocity of only thruster-exiting ions; thus to compute

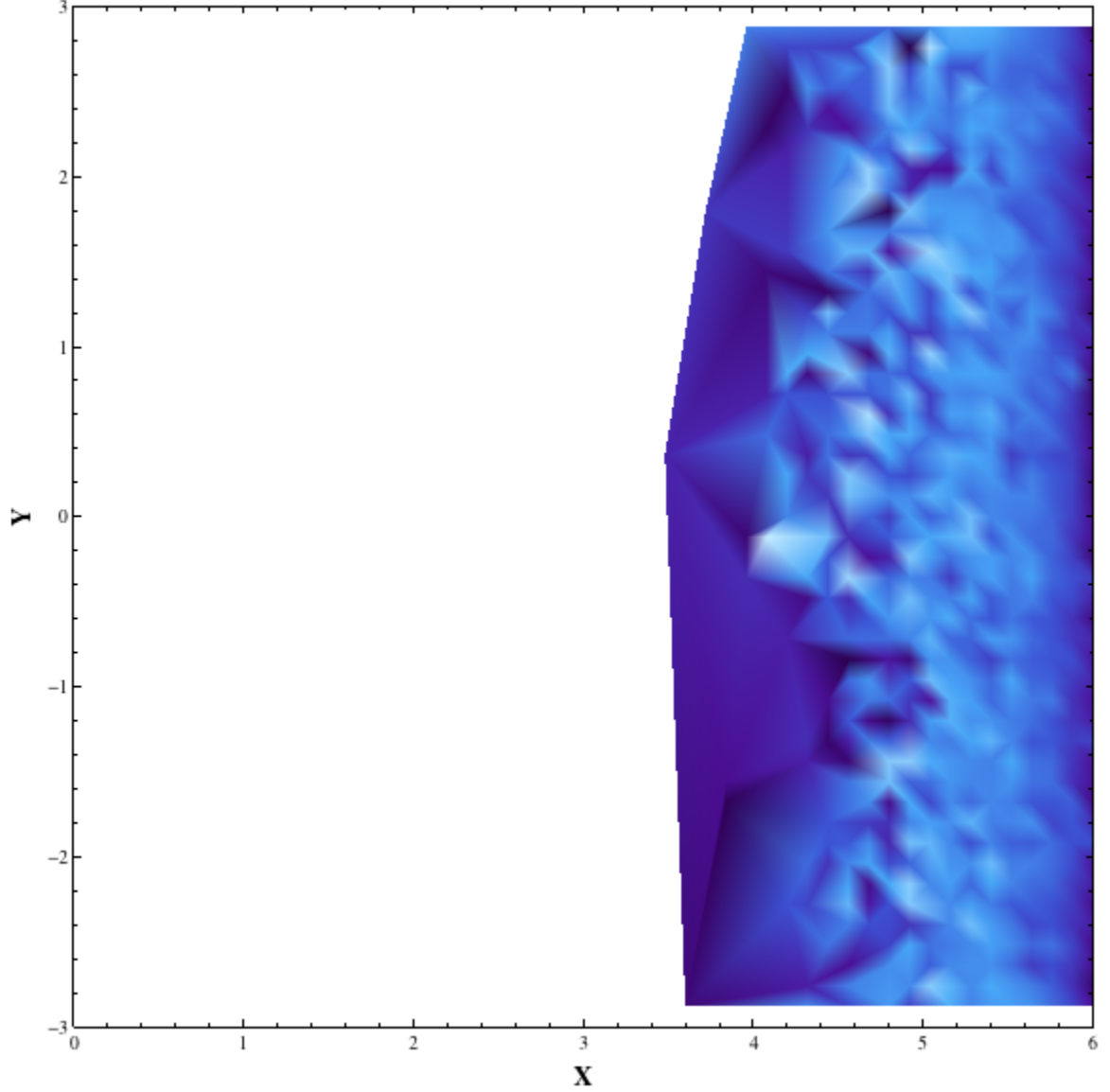


Figure 4.3: Color map of the eventual exit velocity of an ion as a function of its initial position  $(X, Y)$  in the heated, low magnetization case ( $B_0 = 176$  Gauss,  $\bar{\delta} = 0.75$ ). Lighter blue represents higher exit velocity. Empty white space represents ions that are trapped or have been lost to the walls.  $\varepsilon = 10$ ,  $\kappa = 0.16$ ,  $\nu = 1.47$ .

the  $I_{sp}$  of the simulated thruster we must introduce  $\xi_{ex}$  to equation 1.2.2:

$$I_{sp} = \frac{u_{ex}}{g_0} \xi_{ex} \quad (4.2.1)$$

$u_{ex}$  plateaus at around 1000 Gauss, so the optimization of  $I_{sp}$  beyond this magnetization relies on maximizing  $\xi_{ex}$ . This explains why the shape and peak of  $I_{sp}$  in Figure 4.5 and  $\xi_{ex}$  in Figure 4.4 so closely match each other.

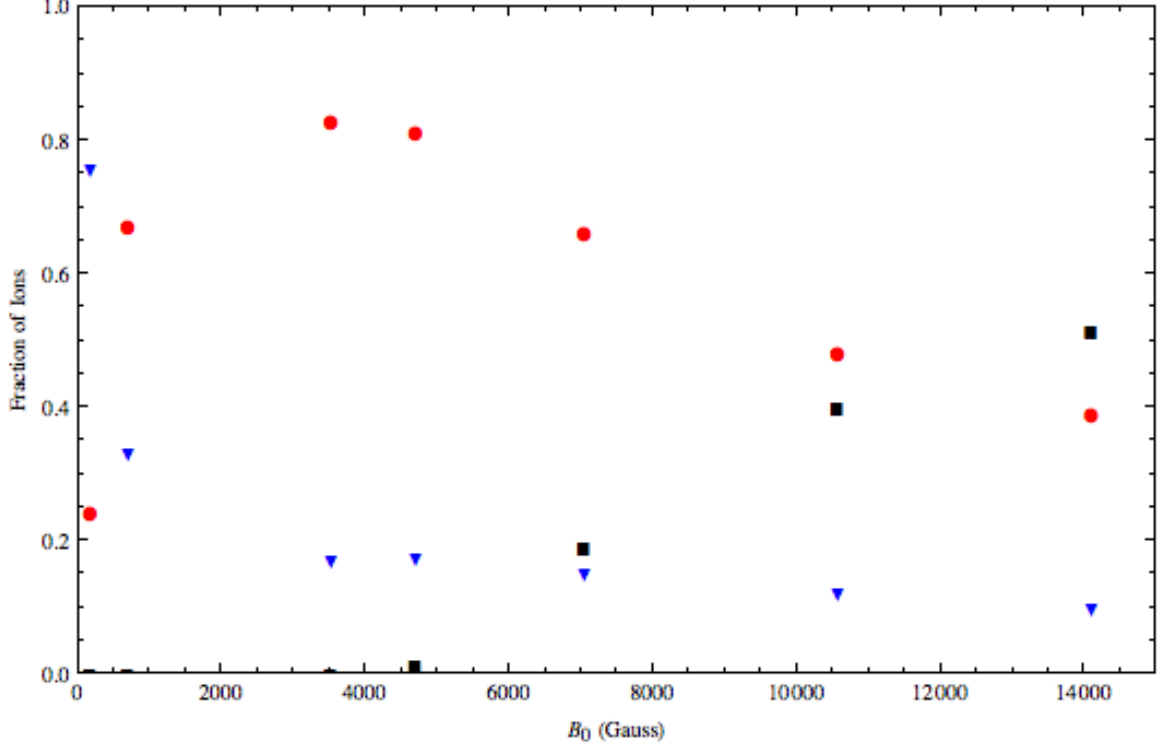


Figure 4.4:  $\xi_{tr}$  (black),  $\xi_{ex}$  (red), and  $\xi_{lost}$  (blue) in the perturbed case at varying field strengths.

These plots show that the performance dropoff occurs at very high magnetic fields that are not physically possible to generate with the coil system constructed in this thesis. The peak  $I_{sp}$  occurs in the vicinity of 5000 Gauss; at 16 Gauss/Amp, our device would require over 300 Amps in a single wire to generate this  $B_0$ . Driving the field strength up effectively makes the thruster larger from the perspective of the ion orbits (by making  $Y_{max}$  larger). However, we can achieve the same effect through more realistic means by scaling up the size of the device in future proof-of-concept attempts. As discussed briefly in section 3.2.3, the device dimensions may be scaled up linearly without affecting the absolute size of  $\delta$ . In the current device,  $\delta = 1.5$  cm and  $y_{max} = 6$  cm, so 1.5 cm of sloped region is occupied on either side of each 3 cm uniform region. If the coils were scaled to  $y_{max} = 20$  cm, the same 1.5 cm would be unusable on either side, making the relative size of the uniform region much larger (17 cm). This accomplishes the same goal of making the thruster larger from the ion orbit perspective; by enlarging the thruster, the benefits of higher magnetization can be gained without requiring unrealistic field strengths.

To test this notion, three simulations are conducted: all utilize the same size magnetic field reversal  $\delta = 1.5$  cm constructed from equation 4.1.1 with  $\sigma = 1.721$ , but

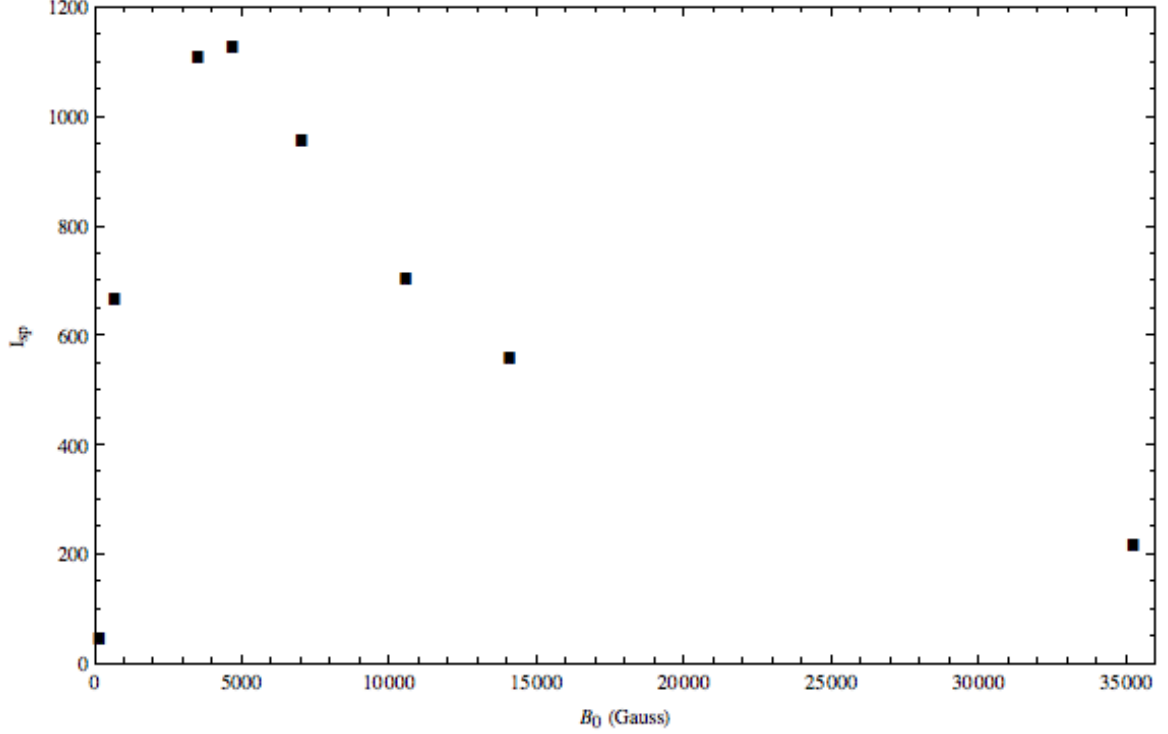


Figure 4.5:  $I_{sp}$  in s versus  $B_0$  in Gauss. There is a clear peak in thruster performance near 5000 Gauss.

the size of the thruster is scaled by changing  $y_{max}$ . One simulation reconstructs the thruster in its actual dimensions ( $y_{max} = 6$  cm) and the others enlarge the thruster ( $y_{max} = 15$  cm,  $y_{max} = 30$  cm). All simulations use the same  $B_0 = 360$  Gauss ( $\bar{r}_L = 1$  cm). Table 4.2 and Figures 4.6 and 4.7 show the results of the simulations. The larger thruster geometries yield substantially better performance showing higher  $\xi_{ex}$ , lower  $\xi_{lost}$ , and better  $I_{sp}$  with increasing size. These results confirm the prediction that the same performance augmentation achieved through higher magnetization can be achieved by enlarging the thruster without the need for inordinate magnetic field strength. Future attempts at a proof-of-concept should utilize this result to appropriately scale up the design.

$y_{max}$	$\delta$	$U_{ex}$	$\xi_{lost}$	$\xi_{ex}$	$\xi_{tr}$	$I_{sp}$
6 cm	1.5 cm	7.497	0.553	0.447	0	237.4 s
15 cm	1.5 cm	17.1	0.265	0.735	0	890.8 s
30 cm	1.5 cm	18.43	0.198	0.802	0	1047.9 s

Table 4.2: Performance results of varying sizes of mathematical reconstructions of the magnetic null topography for  $\bar{r}_L = 1$  cm ( $B_0 = 360$  Gauss).

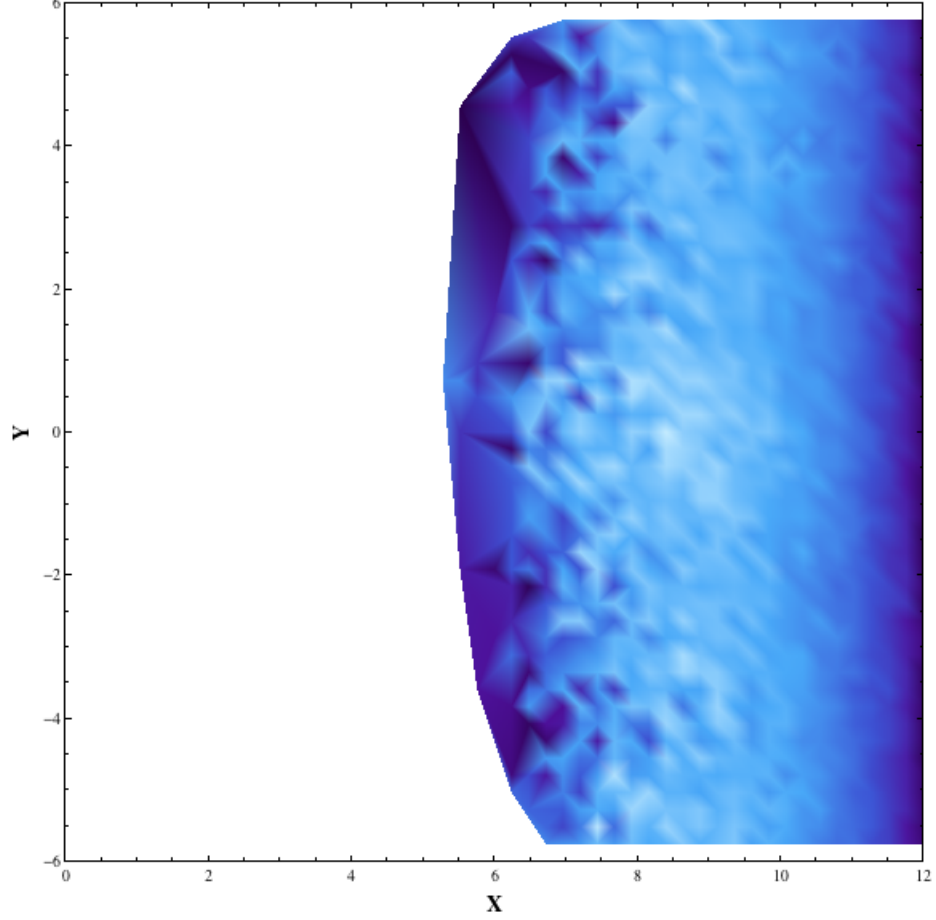


Figure 4.6: Color map of the eventual exit velocity of an ion as a function of its initial position  $(X, Y)$  in the heated case. The field was mathematically defined using  $\sigma = 1.72$  and  $\bar{\delta} = 1.5$  to faithfully reconstruct the thruster magnetic field with  $y_{max} = 6$  cm.

## 4.3 Proof-of-Concept Experiment

### 4.3.1 Experimental Setup

This proof-of-concept thruster was built to integrate with an existing experimental setup for a magnetic nozzle. The setup, including plasma source and generation, is detailed in [16]. Relevant to this thesis is that the 8 cm diameter cylindrical glass tube and coaxial electromagnets were removed from the test stand to be replaced with our duck-billed glass chamber and rectangular flow-perpendicular Helmholtz coils. The plasma source was moved as close to the adapter section in the chamber as possible to eliminate wall losses in the cylindrical section. Plasma injection and generation was unchanged from that used by Little[16]. By altering flow rate of the Argon gas,

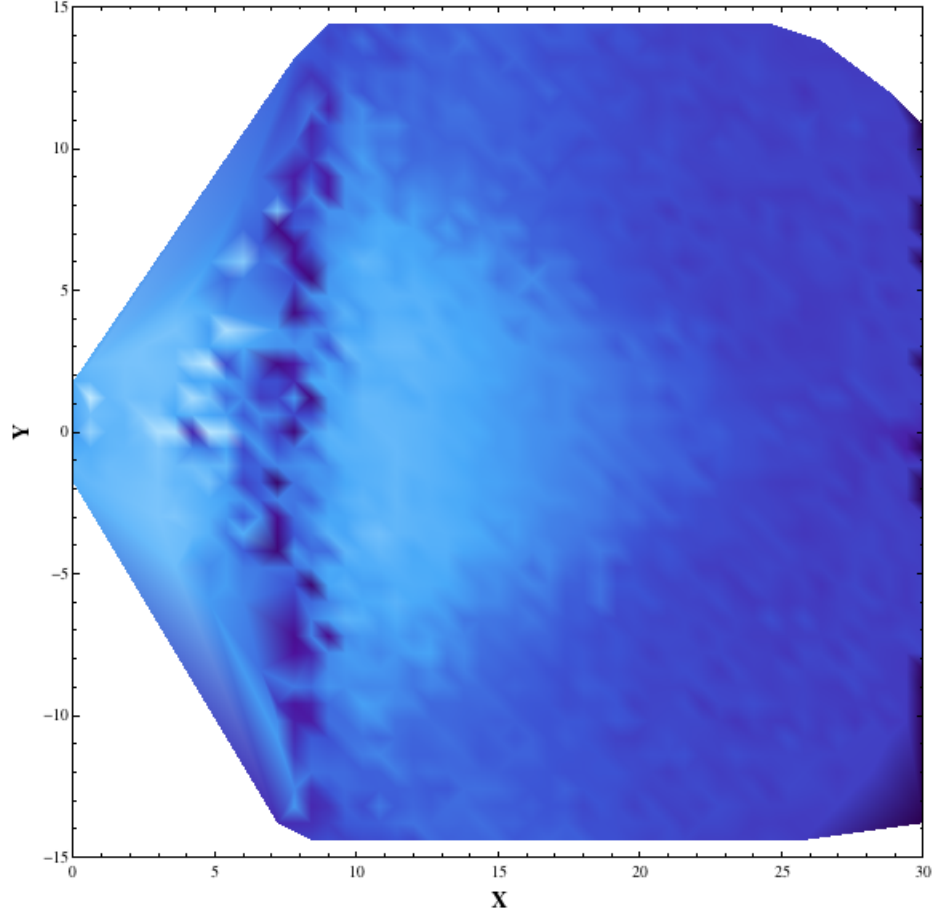


Figure 4.7: Color map of the eventual exit velocity of an ion as a function of its initial position  $(X, Y)$  in the heated case. The field was mathematically defined using  $\sigma = 1.72$  and  $\bar{\delta} = 1.5$  to faithfully reconstruct the thruster magnetic field with  $y_{max} = 15$  cm, a scaled up version of the thruster built for the experiment.

injection densities between  $n \approx 10^{16}$  and  $n \approx 10^{18} \text{ m}^{-3}$  can be achieved. Over two separate runs, a retarding potential analyzer (RPA), Faraday probe, and Langmuir probe were each placed at the thruster exit for taking diagnostics of the ion current. Pictures of the thruster integrated with the experimental setup are found in Appendix C, Figures C.1 to C.3.

### 4.3.2 Experimental Results

Unfortunately, this device was not able to accomplish its goal of proving the feasibility or unfeasibility of the ion current generation by the magnetic null topography. Two unsuccessful attempts were made and are described here; more runs were not possible as the experiment was conducted on time borrowed from the magnetic nozzle

research ongoing in the chamber used.

In the first run, all of the plasma was lost to the chamber walls before reaching beyond  $\sim 2$  cm into the rectangular section. The plasma density, RF power, and  $B_0$  were all varied in attempts to penetrate further into the thruster region to no avail. Images of this attempt are in Appendix C, Figures C.4 to C.6. The RPA was set up to take measurements but did not detect any ions; it was switched out for a Faraday probe in the next run due to the limited sensitivity of the RPA.

To alleviate the massive wall losses experienced, an electromagnetic coil was wound around the section of the chamber between the plasma source and the MagNul coil system. The chamber with windings can be seen in Figure 3.9. The goal of this was to magnetically confine the plasma away from the walls. The coil was 45 turns and produced a field averaging roughly 4 Gauss/Amp at its axis along  $\hat{x}$ . The field it produced in  $\hat{x}$  inside the MagNul thruster chamber was measured at less than 5% of  $B_0$ , having virtually no effect on the rectilinear  $\hat{z}$  field lines.

The confinement did indeed help eliminate wall losses, however the second run still failed. The plasma penetrated visibly further into the rectangular chamber region but was lost entirely within roughly 6 cm. Images from the second attempt are in Appendix C, Figures C.7 to C.9. Neither the Faraday probe nor the Langmuir probe detected any beam exiting the device.

### 4.3.3 Sources of Failure

The most obvious cause of failure was overwhelming loss to the walls. Although the above simulations show  $\xi_{lost}$  on the order of 50% for the highest field strengths possible in the actual experiment ( $\sim 500$  Gauss), the actual loss was much greater than that. Accounting for all previously predicted losses (due to the walls at  $\pm Y_{max}$  and the constriction of the plasma fan), the plasma density should be roughly  $10^{15} \text{ m}^{-3}$  in the plume; however, the Faraday probe with sensitivity to densities of  $10^{14} \text{ m}^{-3}$  at the ion velocities expected did not detect anything. The additional loss then must have been to the walls in  $\pm \hat{z}$ ; that is, the walls separating the plasma from the coils themselves. This could be caused by either divergent field lines or particle drift.

#### Divergent Field Lines

Charged particles orbit in a plane perpendicular to their governing magnetic field line. In our simulations we have assumed rectilinear field lines perfectly along  $\hat{z}$ ; while this is true at the center plane from where the simulation field was measured,

these lines diverge away from the center of the chamber. These bending field lines will cause orbits to tilt out of the  $xy$  plane and thus potentially encounter one of the walls. Figure 4.8 is a simple explanatory depiction. Geometrically we find that the minimum angle  $\theta$  by which a field line must diverge in order to cause an ion with gyroradius  $\rho$  and guiding center at  $Z_{GC}$  to encounter the wall is

$$\theta = \sin^{-1} \frac{Z_{max} - Z_{GC}}{\rho} \quad (4.3.1)$$

where  $Z_{max}$  is the  $Z$ -position of the wall (analogous to  $Y_{max}$ ) and is equal to  $z_{max}/\bar{r}_L$  (recalling that  $z_{max} = 0.6$  cm). Intuitively the allowable tilt angle gets smaller as  $Z_{GC}$  nears the wall; unfortunately, the divergence increases approaching the wall. Figure 4.9 shows the divergence angle of the field lines (computed from data extracted by ANSYS Maxwell simulations) and  $\theta$ . The field divergence causes roughly 13% of the plasma to be lost for  $B_0 = 240$  Gauss. This fraction increases with weakening field since the ion gyroradius gets larger.

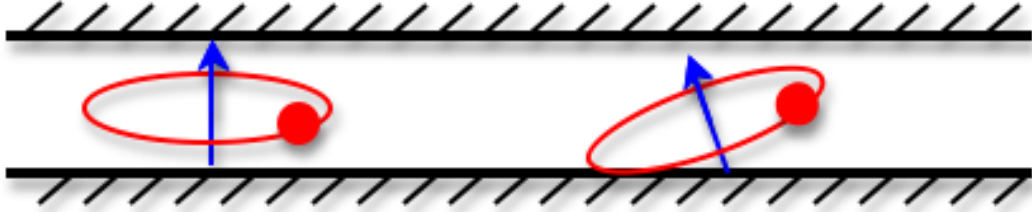


Figure 4.8: Magnetic field lines (blue) diverging away from  $\hat{z}$  tilt the Larmor orbits of ions, increasing their chance of hitting a wall.

## Particle Drift

Since the field lines in the MagNul are solely along  $\hat{z}$ , any ion entering the uniform field region with an initial  $z$ -parallel velocity  $v_z$  will maintain that velocity. If the time it takes to drift to  $\pm Z_{max}$  is shorter than the residence time, the ion will be lost to the wall. It is likely that many ions meet this condition due to the very small width of the chamber. In the first trial of the experiment, this drift would arise from thermal motion of the plasma in  $\pm\hat{z}$ .

In the second run, things are slightly more complicated. The field lines in the confinement region are  $x$ -aligned while those in the thruster region are  $z$ -aligned.



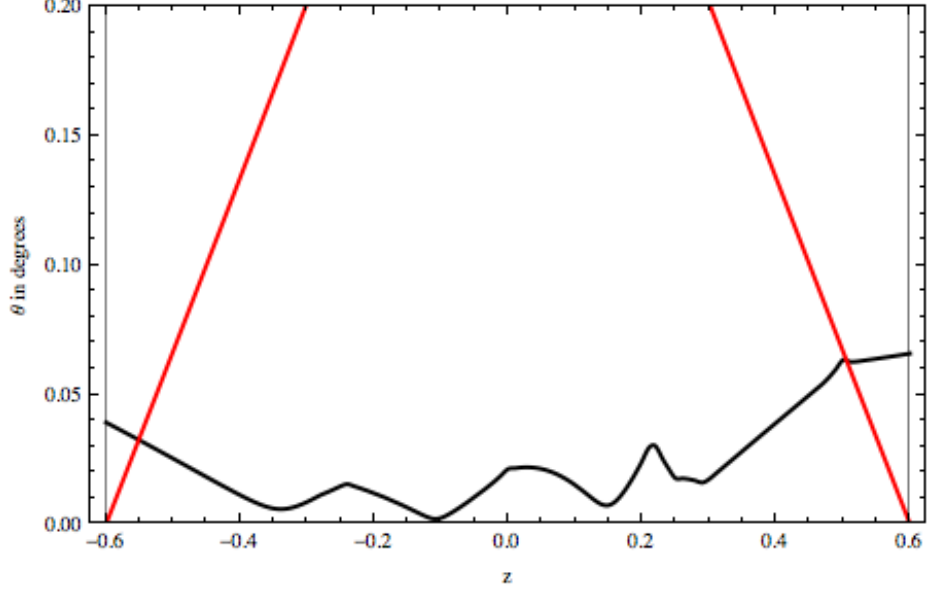


Figure 4.9:  $\theta(z)$  (red) and the actual divergence of the uniform field lines (black) for  $\bar{r}_L = 1.5$  cm. The field divergence only exceeds  $\theta$  very close to the walls, causing roughly 13% of the plasma to be lost.

Magnetic field lines cannot intersect, therefore the magnetic confinement lines must either attach to or diverge away from the MagNul field lines. For those lines that diverge away, ions orbiting will follow their contour and hit a wall before entering the thruster region. The only lines that reach into the MagNul are those on the null plane, in which case the orbiting ions are not being guided by the dynamics of the MagNul but rather the magnetic nozzle created by the confinement coil. Ions that are able to transition between their confinement orbit in the  $yz$  plane and a MagNul orbit in the  $xz$  plane would need to do so with minimal final  $v_z$  to avoid encountering a wall via drift. After placing so many conditionals on a thruster-exiting ion in the magnetically confined case, it is easy to imagine why there was no detectable ion beam despite preventing many of the thermal wall losses in the plasma generation region.

## 4.4 Future Work

Future research could aim to accomplish the proof-of-concept in a variety of ways. Discussed already is to increase the size of the thruster using the same geometry; that is, maintain the rectangular Helmholtz style of the device and increase the spacing to allow a larger chamber. Simulations and predictions regarding wall losses indicate

that this has the potential for success. Such a device could be similarly implemented in an existing experimental setup.

Another option is to build a dedicated experiment setting for the MagNul in which geometric constraints of the vacuum chamber and test stand would not hinder the design of a device. Doing so would allow for a larger version of the device built for this thesis or even an entirely new geometry. For instance, an annular geometry may be desirable since almost any thruster that comes to fruition must be cylindrical in shape. An example of what that might look like is shown in Figure 4.10. Field-generating coils are placed around a ring to create the magnetic null topography where the null “plane” is actually a cylindrical sheet and the uniform regions occupy radius space outside and inside of it. The device depicted is merely a preliminary concept: obvious problems are protecting the coils from the plasma flow and determining the current in the inner and outer coils such that they produce equal strength magnetic fields in their respective uniform regions.

## 4.5 Concluding Remarks

This thesis was successful in proving the feasibility of generating the magnetic null topography by constructing an electromagnetic coil system to generate the field. Measurements showed that it closely followed the theoretical construct introduced by Jorns[12] in the reversal and uniform regions. Due to test stand constraints on the size of the device, the proof-of-concept experiment failed in both attempts. Overwhelming plasma loss to the chamber walls was caused by both the lack of unimpeded space within the thruster and the limited capability of field strength in the uniform region. In simulations, increasing the size of the thruster relative to the initial ion RMS Larmor radius improves the performance of the device. This can be achieved either by strengthening the uniform magnetic field to tighten the orbits or, more realistically, by increasing the overall size of the device which does not affect the size of the magnetic reversal.

A revised theoretical construct of the magnetic null topography using a scaling parameter  $\sigma$  allows us to mathematically describe a field with any desired reversal width for any desired wave parameters. This proves useful in conducting simulations of potential device geometries with a theoretical field that closely follows (visually and definitionally) what the device itself would generate.

Though the predicted ability of the MagNul to produce an ion current was not confirmed experimentally, neither was it disproven. The experimental shortcomings

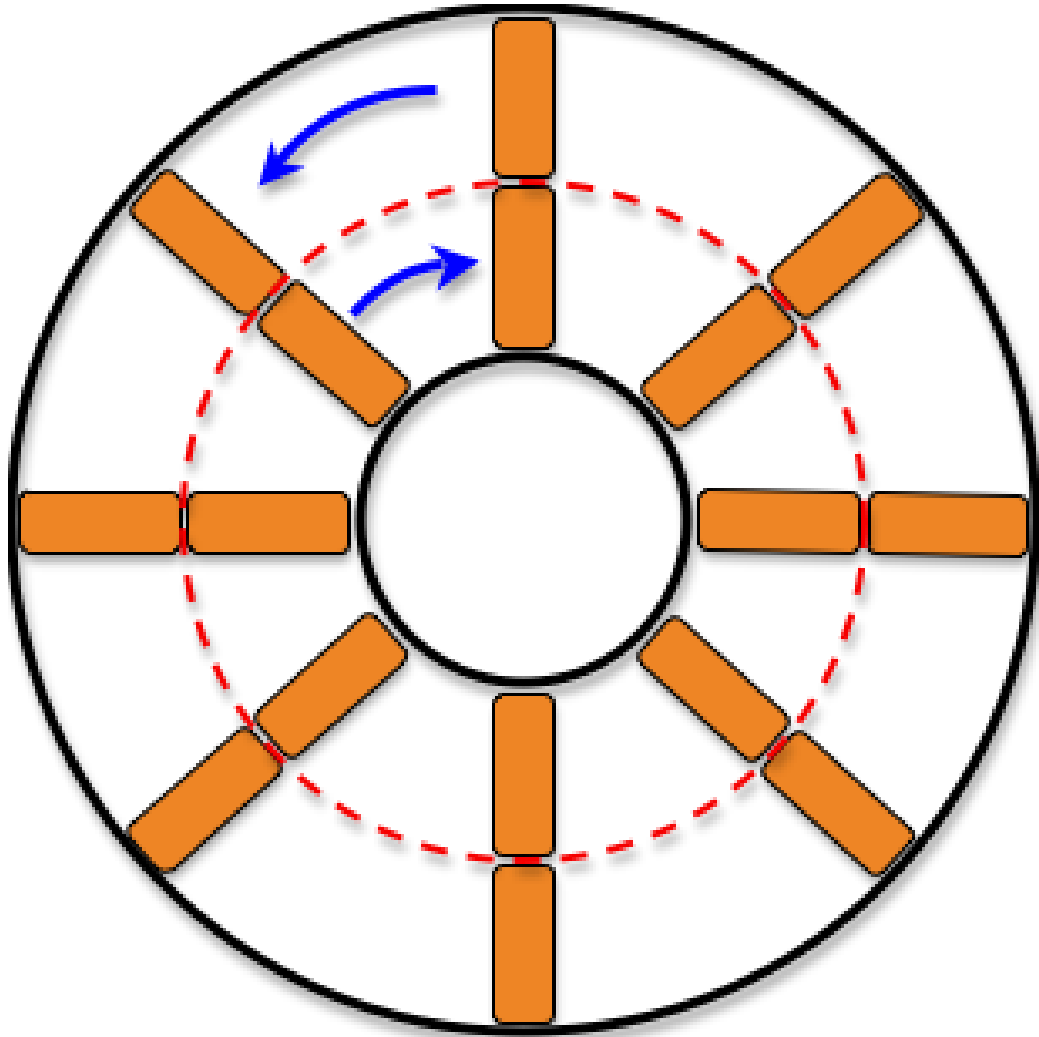


Figure 4.10: View along the thrust axis of a potential annular MagNul. Field-generating coils (orange) placed around a ring generate a cylindrical null sheet (red). Blue arrows indicate direction of field lines.

and simulations of a device with the physically generated field both indicate that a thruster with a chamber larger in  $\hat{y}$  and  $\hat{z}$  shows promise for success.

# Bibliography

- [1] V. P. Ageyev and V. G. Ostrovsky. High-Current Stationary Plasma Accelerator of High Power. In *23rd International Electric Propulsion Conference*, 1993.
- [2] E. Ahedo, J. M. Gallardo, and M. Martnez-Sanchez. Effects of the radial plasma-wall interaction on the Hall thruster discharge. *Physics of Plasmas*, 10(8):3397–3409, 2003.
- [3] D. Benisti, A. K. Ram, and A. Bers. Ion dynamics in multiple electrostatic waves in a magnetized plasma. I. Coherent acceleration. *Physics of Plasmas*, 5(9):3224–3232, 1998.
- [4] D. Benisti, A. K. Ram, and A. Bers. Ion dynamics in multiple electrostatic waves in a magnetized plasma. II. Enhancement of the acceleration. *Physics of Plasmas*, 5(9):3233–3241, 1998.
- [5] F. F. Chen. *Introduction to Plasma Physics and Controlled Fusion, Volume 1: Plasma Physics*. Plenum Press, New York, second edition, 1984.
- [6] P.-K. Chia, L. Schmitz, and R. W. Conn. Stochastic ion behavior in subharmonic and superharmonic electrostatic waves. *Physics of Plasmas*, 3(5):1545–1568, 1996.
- [7] M. Feldman and E. Y. Choueiri. Electron Dynamics in a Beating Electrostatic Wave Magnetic Null Thruster. In *48th AIAA/ASME/SAE/ASEE Joint Propulsion Conference & Exhibit*, Reston, Virginia, July 2012. American Institute of Aeronautics and Astronautics.
- [8] FerroxCube. 3C97 Extreme Ferrites Data Sheet, 2010.
- [9] B. G. Gardineer. BEW Ion Trajectories (Rho), 2011.

- [10] B. G. Gardineer, B. Jorns, and E. Y. Choueiri. Simulations of Direct Ion Acceleration with Beating Electrostatic Waves. In *International Electric Propulsion Conference*, 2011.
- [11] R. G. Jahn. *Physics of Electric Propulsion*. McGraw-Hill, Inc., New York, 1968.
- [12] B. Jorns and E. Y. Choueiri. A Plasma Propulsion Concept Based on Direct Ion Acceleration with Beating Electrostatic Waves. In *46th AIAA/ASME/SAE/ASEE Joint Propulsion Conference & Exhibit*, pages 1–19, 2010.
- [13] C. F. F. Karney and A. Bers. Stochastic Ion Heating by a Perpendicularly Propagating Electrostatic Wave. *Physical Review Letters*, 39(9):550–554, 1977.
- [14] J. Köhler, J. Bejhed, H. Kratz, F. Bruhn, U. Lindberg, K. Hjort, and L. Stenmark. A hybrid cold gas microthruster system for spacecraft. *Sensors and Actuators A: Physical*, 97-98:587–598, Apr. 2002.
- [15] A. S. Landsman, S. A. Cohen, and A. H. Glasser. Regular and stochastic orbits of ions in a highly prolate field-reversed configuration. *Physics of Plasmas*, 11(3):947–957, 2004.
- [16] J. M. Little and E. Y. Choueiri. Plasma transport in a converging magnetic field with applications to helicon plasma thrusters. In *33rd International Electric Propulsion Conference*, 2013.
- [17] D. Manzella, R. Jankovsky, and R. Hofer. Laboratory Model 50 kW Hall Thruster. In *38th Joint Propulsion Conference*, 2002.
- [18] NASA. J-2 Engine Fact Sheet, 1968.
- [19] W. Peter and N. Rostoker. Theory of Plasma Injection Into a Magnetic Field. *Physics of Fluids*, 25(4):730–735, 1982.
- [20] A. K. Ram, A. Bers, and D. Benisti. Ionospheric ion acceleration by multiple electrostatic waves. *Journal of Geophysical Research*, 103(A5):9431–9440, 1998.
- [21] K. Sankaran, L. Cassady, A. D. Kodys, and E. Y. Choueiri. A survey of propulsion options for cargo and piloted missions to Mars. *Annals of the New York Academy of Sciences*, 1017:450–467, May 2004.

- [22] J. S. Sovey and M. A. Manteniekst. Performance and Lifetime Assessment of Magnetoplasmdynamic Arc Thruster Technology. *Journal of Propulsion*, 7(1):71–83, 1991.
- [23] R. Spektor and E. Y. Choueiri. Ion acceleration by beating electrostatic waves: domain of allowed acceleration. In *International Electric Propulsion Conference*, 2001.
- [24] P. J. Wilbur, R. G. Jahn, and F. C. Curran. Space electric propulsion plasmas. *IEEE Transactions on Plasma Science*, 19(6):1167–1179, 1991.

# Appendix A

## Calculation of Plasma Fan

We wish to calculate the “fan” of plasma that reaches the rectangular exit of the chamber from the plasma injection hole. From the hole to the exit plane of the chamber is  $x = 18$  cm; to the top and bottom edges of the exit is  $y = \pm 6$  cm; to the left and right edges is  $z = \pm 0.6$  cm. We can assume the injection-induced momentum of the plasma is unimpeded by the magnetic field because  $\gamma \gg 1$  at our possible densities and field strengths[19]; thus, we can find the fraction of the plasma within the fan from the 3D Maxwellian velocity distribution.

The average  $x$ -velocity of ions is[5]

$$|\bar{v}_x| = \sqrt{\frac{2k_B T}{\pi m}}$$

where  $k$  is Boltzmann’s constant,  $T$  is the average ion temperature, and  $m$  is the ion mass. This gives an average residence time  $t$  of

$$t = \frac{x}{|\bar{v}_x|} = \frac{18}{|\bar{v}_x|}$$

recalling that  $x = 18$  cm. Since there is no wall in  $\hat{\mathbf{x}}$ , there is no upper restriction on the  $x$ -velocity of a thruster-exiting ion, i.e.  $v_x \in [0, \infty)$ . Ions with  $y$ - and  $z$ -velocities fast enough to encounter a wall before reaching the thruster exit will be lost; therefore, our plasma fan excludes all ions outside this velocity profile. In other words, an ion within the fan must have a slow enough  $v_y$  and  $v_z$  that it does not encounter a wall

within the residence time  $t$ . Thus the upper bounds on  $v_y$  and  $v_z$  are

$$\begin{aligned} v_{y,max} &= \pm \frac{y}{t} = \pm \frac{6}{18/|v_x|} = \pm \frac{1}{3}|v_x| \\ v_{z,max} &= \pm \frac{z}{t} = \pm \frac{0.6}{18/|v_x|} = \pm \frac{1}{30}|v_x| \end{aligned}$$

The range of velocities within the thruster-exiting fan is then

$$\begin{aligned} v_x &\in [0, \infty) \\ v_y &\in \left[ -\frac{1}{3}|v_x|, \frac{1}{3}|v_x| \right] \\ v_z &\in \left[ -\frac{1}{30}|v_x|, \frac{1}{30}|v_x| \right] \end{aligned}$$

To compute the fraction of ions  $p$  within this fan, we take the integral

$$p = \int_{-\mathbf{v}_{max}}^{\mathbf{v}_{max}} \hat{f}(\mathbf{v}) d^3v$$

where  $\hat{f}(\mathbf{v})$  is a probability function of velocity  $\mathbf{v}$  and  $\pm\mathbf{v}_{max}$  are the bounds on velocity discussed above. Chen[5] expands this integral using the Maxwellian probability function to

$$p = \left( \frac{m}{2\pi k_B T} \right)^{3/2} \int_{-v_{max}}^{v_{max}} \exp \left[ -\frac{v^2}{v_{th}^2} \right] dv$$

where  $v_{th}$  is the thermal ion velocity,  $\sqrt{\frac{2k_B T}{m}}$ . Expanding further to component velocities, we have

$$p = \left( \frac{m}{2\pi k_B T} \right)^{3/2} \int_{-v_{x,max}}^{v_{x,max}} \int_{-v_{y,max}}^{v_{y,max}} \int_{-v_{z,max}}^{v_{z,max}} \exp \left[ -\frac{v_x^2 + v_y^2 + v_z^2}{v_{th}^2} \right] dv_z dv_y dv_x$$

We plug in our values of  $|v_{x,max}| = \infty$ ,  $|v_{y,max}| = \frac{1}{3}|v_x|$ , and  $|v_{z,max}| = \frac{1}{30}|v_x|$  to the above integral to yield

$$p = \left( \frac{m}{2\pi k_B T} \right)^{3/2} 2 \int_0^\infty \int_{-\frac{1}{3}|v_x|}^{\frac{1}{3}|v_x|} \int_{-\frac{1}{30}|v_x|}^{\frac{1}{30}|v_x|} \exp \left[ -\frac{v_x^2 + v_y^2 + v_z^2}{v_{th}^2} \right] dv_z dv_y dv_x$$

where we have multiplied by 2 to account for the fact that our plasma expands hemispherically towards  $\hat{\mathbf{x}}$  instead of spherically in all directions as Chen assumes.



For Argon gas ( $m = 6.63 \times 10^{-26}$  kg) at  $T = 0.1$  eV (1160 Kelvin),  $|v_x^-| = 392$  m/s and  $v_{th} = 695$  m/s. This makes our integral

$$p = 5.35 \times 10^{-10} \times 2 \int_0^\infty \int_{-130.7}^{130.7} \int_{-13.1}^{13.1} \exp \left[ -\frac{v_x^2 + v_y^2 + v_z^2}{(695)^2} \right] dv_z dv_y dv_x = 0.00445$$

Thus, 99.5% of the plasma is lost to the walls due to thermal expansion from the plasma source.

# Appendix B

## Derivation of Scaling Parameter $\sigma$

We are motivated by the maximum allowable  $\nabla B$  drift velocity  $V_{d,max}$  of an ion for it to be considered within a uniform field region. This definition is

$$V_{d,max} = \frac{\nu}{2\tau_{max}}$$

We wish to equate this to an expression for  $V_{d,max}$  in terms of the scaling parameter  $\sigma$  and the desired  $\bar{\delta}$  it will reconstruct. The expression for  $\nabla B$  drift velocity  $V_d$  is

$$\mathbf{V}_d = \frac{1}{2}\rho V_\perp \frac{\mathbf{B}(Y) \times \nabla \mathbf{B}(Y)}{B^2(Y)}$$

Since  $\mathbf{B}(Y)$  is in  $\hat{\mathbf{z}}$  and  $\nabla \mathbf{B}(Y)$  is in  $\hat{\mathbf{y}}$ , the two are orthogonal and we can proceed computing the scalar  $V_d$  knowing it is in  $\hat{\mathbf{x}}$ .  $B(Y)$  is defined as  $\tanh \frac{\sigma Y}{\bar{\delta}}$ , so  $V_d$  becomes

$$\begin{aligned} V_d &= \frac{1}{2}\rho V_\perp \left( \frac{\frac{\sigma}{\bar{\delta}} \tanh \frac{\sigma Y}{\bar{\delta}} \operatorname{sech}^2 \frac{\sigma Y}{\bar{\delta}}}{\tanh^2 \frac{\sigma Y}{\bar{\delta}}} \right) \\ &= \frac{1}{2}\rho V_\perp \left( \frac{\frac{\sigma}{\bar{\delta}} \tanh \frac{\sigma Y}{\bar{\delta}} (1 - \tanh^2 \frac{\sigma Y}{\bar{\delta}})}{\tanh^2 \frac{\sigma Y}{\bar{\delta}}} \right) \\ &= \frac{\rho V_\perp \sigma}{2\bar{\delta}} \left( \frac{\tanh \frac{\sigma Y}{\bar{\delta}} - \tanh^3 \frac{\sigma Y}{\bar{\delta}}}{\tanh^2 \frac{\sigma Y}{\bar{\delta}}} \right) \\ &= \frac{\rho V_\perp \sigma}{2\bar{\delta}} \left( \coth \frac{\sigma Y}{\bar{\delta}} - \tanh \frac{\sigma Y}{\bar{\delta}} \right) \end{aligned}$$

Substituting hyperbolic trigonometric identities in for  $\tanh$  and  $\coth$ , we can simplify the term in parentheses (for simplicity we write  $\frac{\sigma Y}{\bar{\delta}}$  as  $x$ ):

$$\begin{aligned}
\coth x - \tanh x &= \frac{e^x + e^{-x}}{e^x - e^{-x}} - \frac{e^x - e^{-x}}{e^x + e^{-x}} \\
&= \left( \frac{e^x + e^{-x}}{e^x - e^{-x}} \right) \frac{e^x + e^{-x}}{e^x - e^{-x}} - \left( \frac{e^x - e^{-x}}{e^x - e^{-x}} \right) \frac{e^x - e^{-x}}{e^x + e^{-x}} \\
&= \frac{e^{2x} + 2 + e^{-2x}}{e^{2x} - e^{-2x}} - \frac{e^{2x} - 2 + e^{-2x}}{e^{2x} - e^{-2x}} \\
&= \frac{4}{e^{2x} - e^{-2x}} \\
&= 2\text{csch}(2x)
\end{aligned}$$

Now we have

$$V_d = \frac{\rho V_{\perp} \sigma}{\bar{\delta}} \text{csch} \frac{2\sigma Y}{\bar{\delta}}$$

For an ion at RMS velocity  $V_{\perp} = 1$ ,  $\rho = 1$ . At  $V_d = V_{d,max} = \nu/2\tau_{max}$ ,  $Y = \bar{\delta}$  by definition. We therefore arrive at the implicit definition of  $\sigma$  for an RMS orbiting ion:

$$\frac{\nu \bar{\delta}}{2\tau_{max}} = \sigma \text{csch}(2\sigma)$$

# Appendix C

## Experiment Pictures

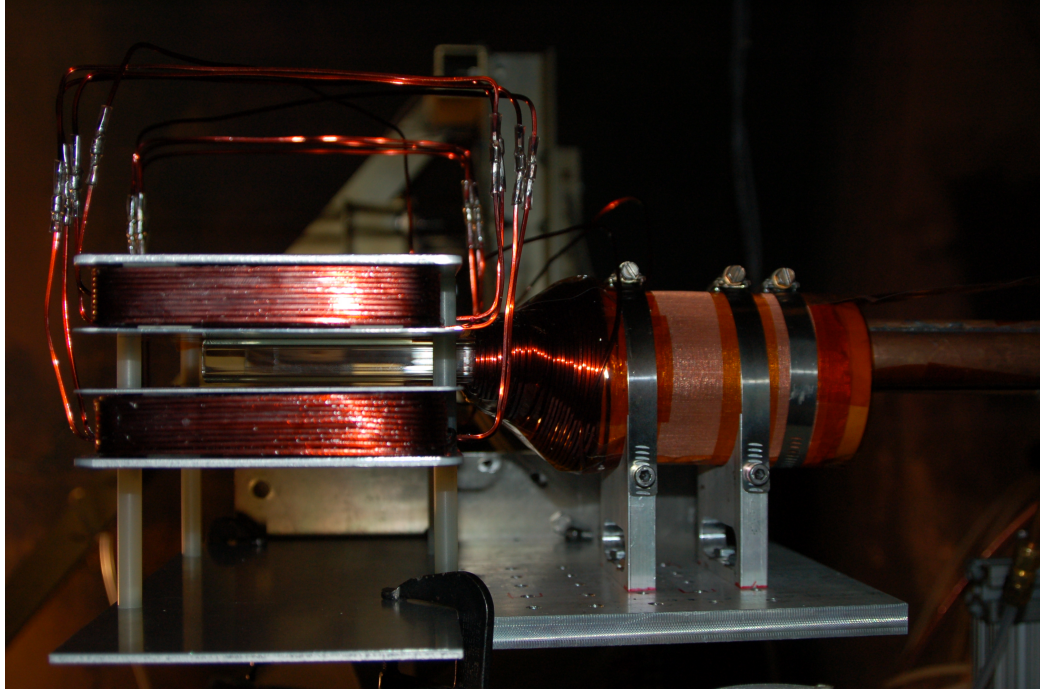


Figure C.1: Side view from  $+\hat{y}$  of thruster setup on test stand. Plasma flows from right to left in this image. Plasma source and RF antenna can be seen entering the cylindrical section of the duck-billed glass tube. The injection backplate lies just to the right of the beginning of the confinement windings. Due to an error made by the glass-blowing shop, the chamber extends about 1" short of the end of the magnets.

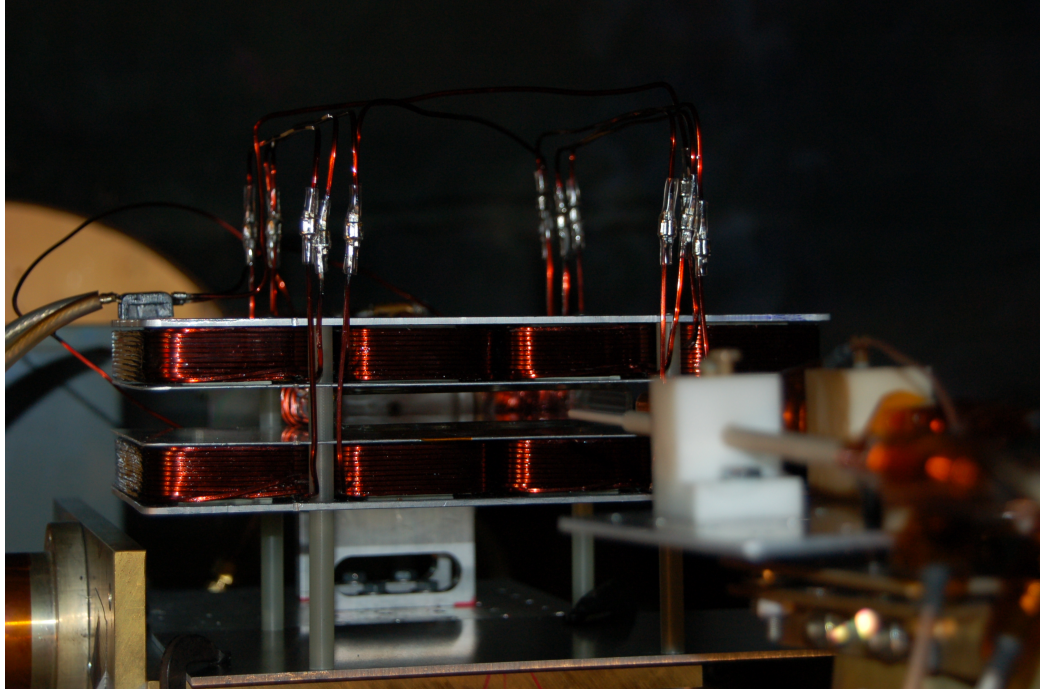


Figure C.2: View from the exit-side of the thruster. Plasma would be exiting towards the viewer in this image.

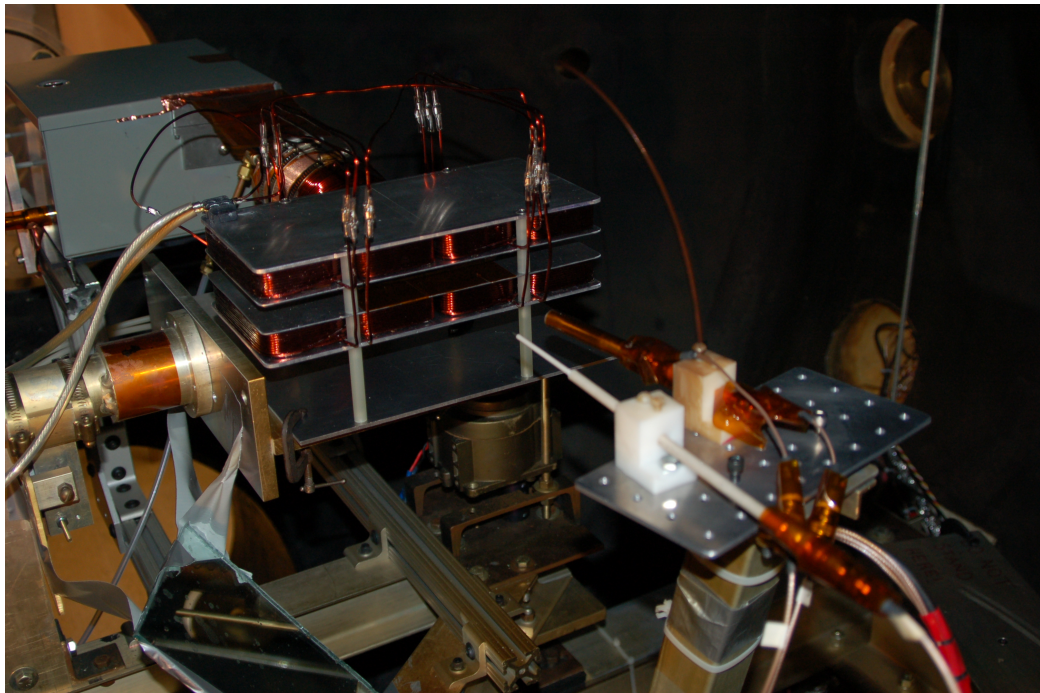


Figure C.3: View from exit-side of the thruster showing the plasma source and generator (top left), the thruster chamber and field generator, and Faraday and Langmuir probes in plume region.



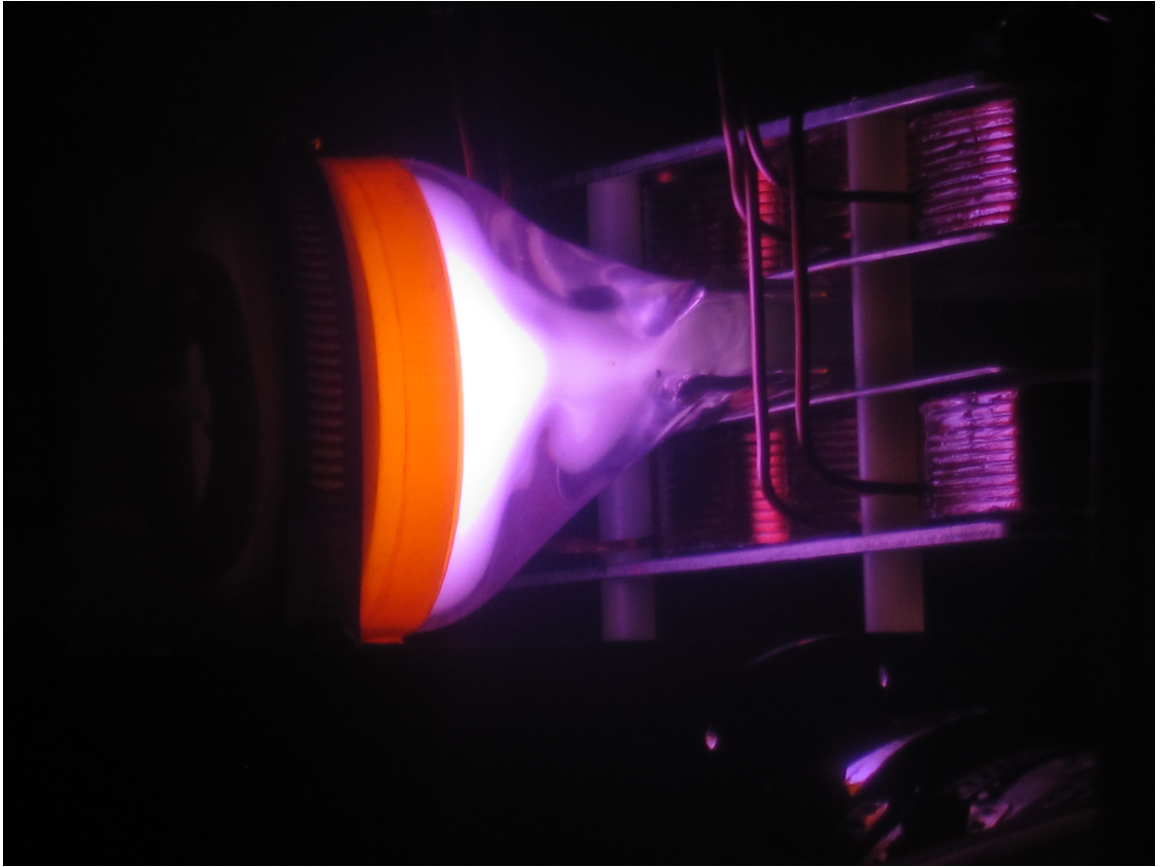


Figure C.4: Plasma injection into the thruster region without magnetic confinement coils. Image taken from the  $-\hat{y}$  side.

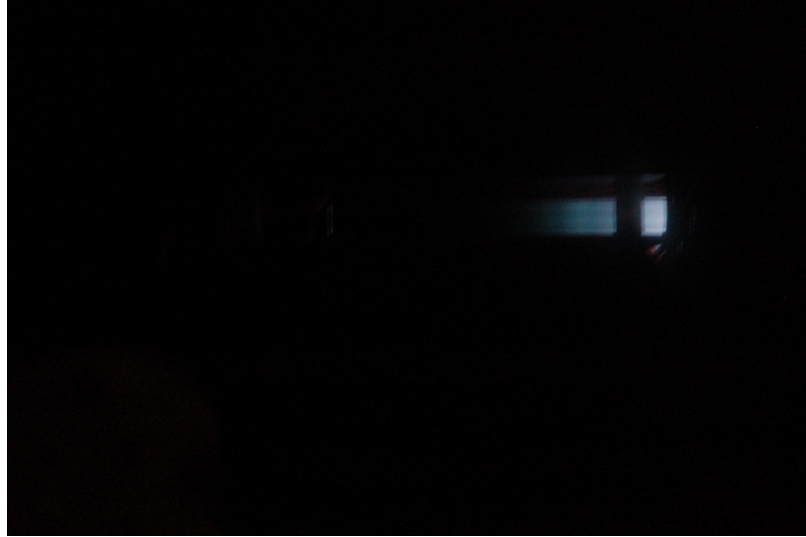


Figure C.5: Plasma penetration into the thruster region at low density and RF power without magnetic confinement coils. This image was taken from  $+\hat{y}$ ; plasma flow is from right to left. The gray streak is the plasma inside the rectangular chamber region; the G10 standoff partially obscuring the plasma, about 1 cm wide, gives a sense of the length scale. All plasma is lost after roughly 2 cm.

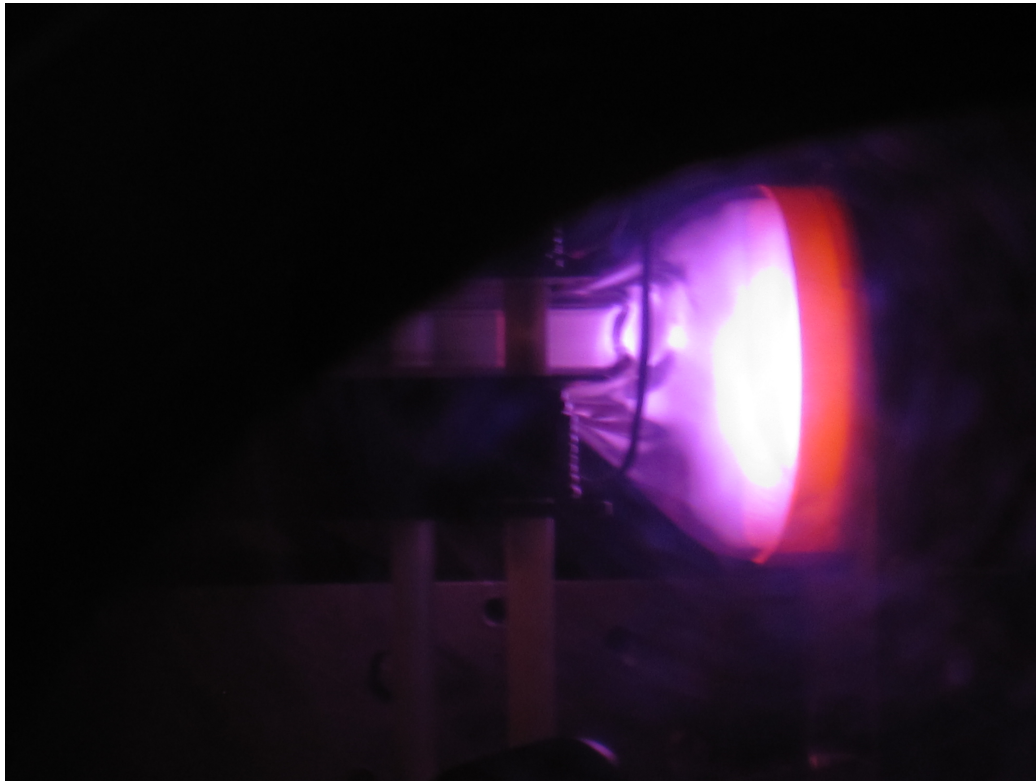


Figure C.6: Plasma injection into the thruster region without magnetic confinement coils. Image taken from the  $+\hat{y}$  side. The G10 standoff obscuring the plasma in Figure C.5 can be seen more clearly in this image, taken from the same vantage point.

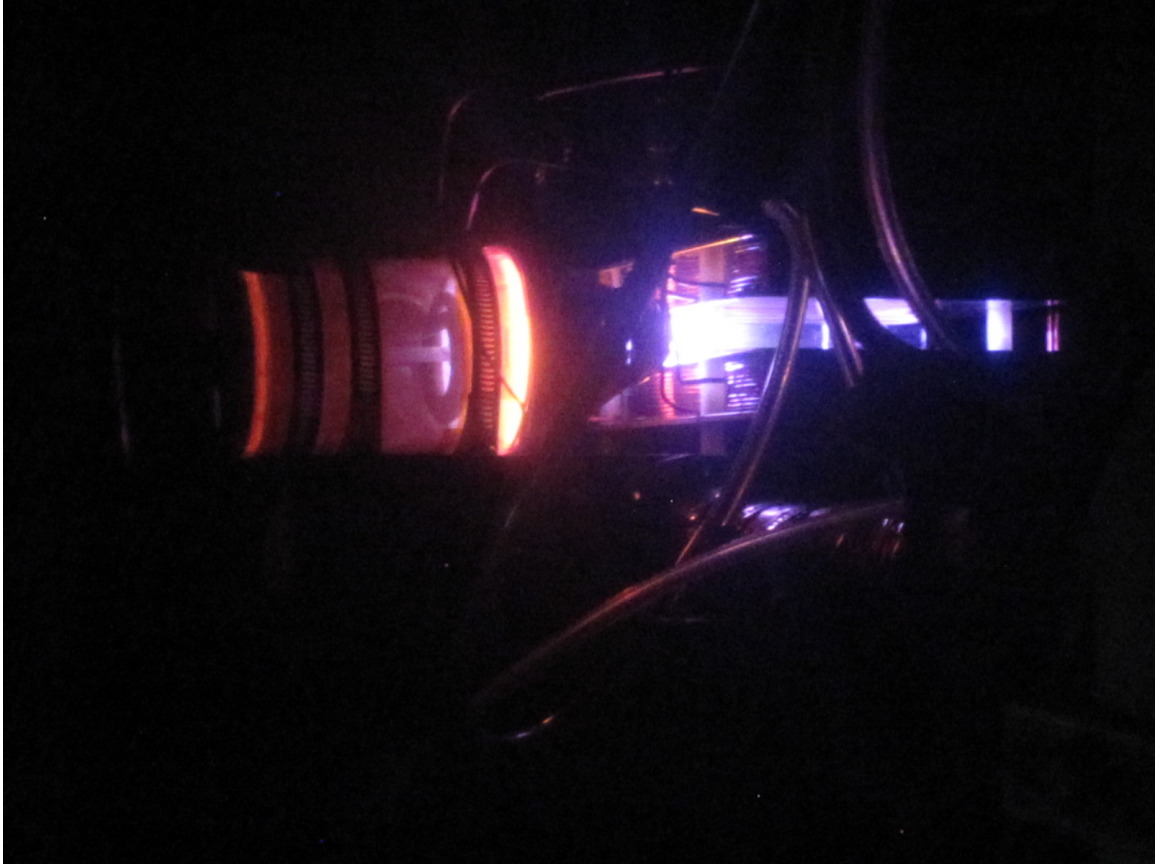


Figure C.7: Plasma injection into the thruster chamber with magnetic confinement coil. The RF antenna sitting behind the backplate inside the cylindrical section can be seen clearly. Taken from the  $-\hat{y}$  side.



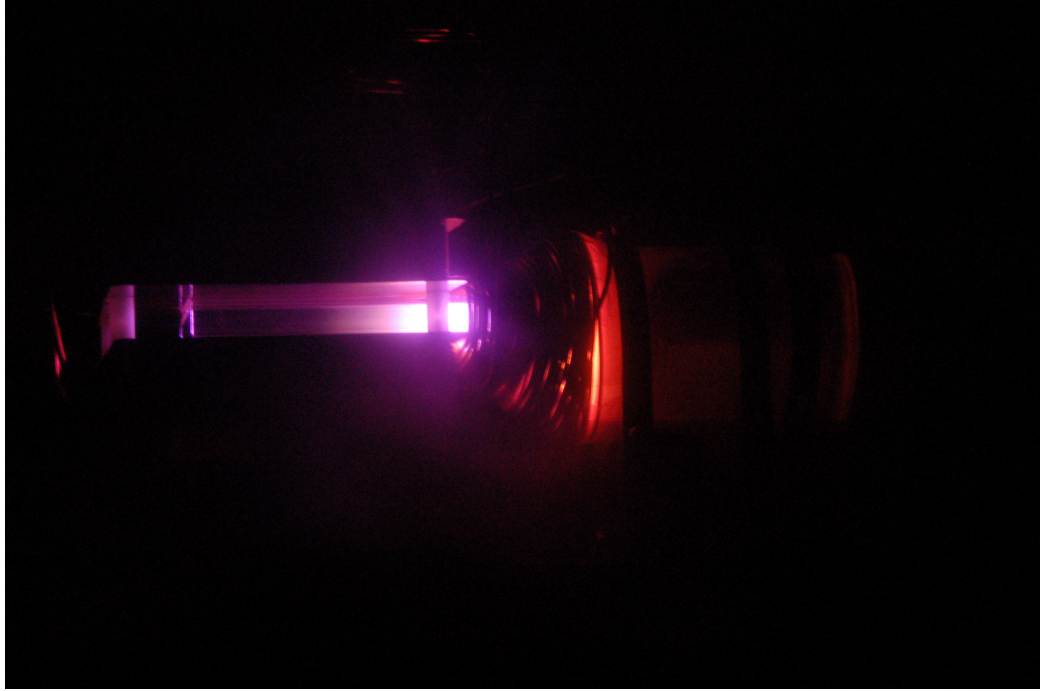


Figure C.8: View from  $+\hat{y}$  of the plasma penetration into the thruster region. The plasma makes it about halfway through the chamber (or 6 cm) before being completely lost to the walls.

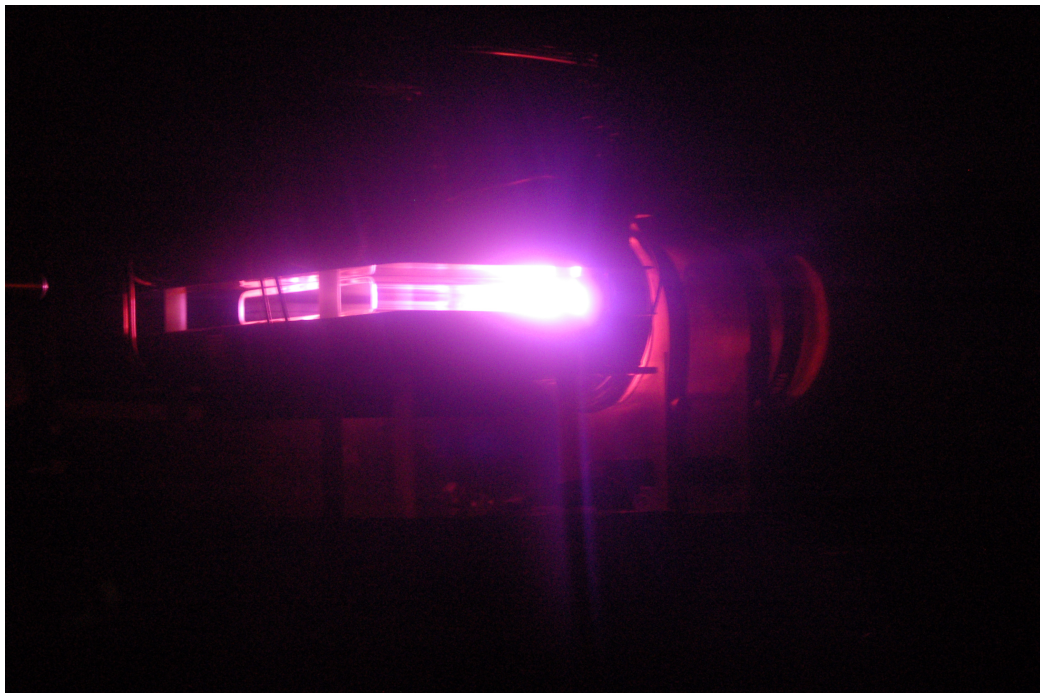


Figure C.9: Operation of the MagNul with magnetic confinement at high RF power and density.